Contract No:

This document was prepared in conjunction with work accomplished under Contract No. DE-AC09-08SR22470 with the U.S. Department of Energy (DOE) Office of Environmental Management (EM).

Disclaimer:

This work was prepared under an agreement with and funded by the U.S. Government. Neither the U. S. Government or its employees, nor any of its contractors, subcontractors or their employees, makes any express or implied:

1) warranty or assumes any legal liability for the accuracy, completeness, or for the use or results of such use of any information, product, or process disclosed; or
2) representation that such use or results of such use would not infringe privately owned rights; or
3) endorsement or recommendation of any specifically identified commercial product, process, or service.

Any views and opinions of authors expressed in this work do not necessarily state or reflect those of the United States Government, or its contractors, or subcontractors.

Final Report

Project Title:	Fundamental Corrosion Studies in High-Temperature Molten Salt Systems for Next Generation Concentrated Solar Power Systems
Project Period:	10/01/12 – 9/30/15
Budget Period:	Phase 3; 10/01/14 – 9/30/15
Budget Period Budget:	$1,272,821
Reporting Period:	Final Report
Reporting Frequency:	Final Report
Submission Date:	01/15/16
Recipient:	Savannah River National Laboratory
Address:	Savannah River Site Aiken, SC 29808
Award Number:	Garcia-Diaz_A
Project Team:	The University of Alabama University of South Carolina
Contacts:	
Principal Investigator:	Brenda L. Garcia-Diaz Principal Engineer Phone: (803) 725-9978 Email: brenda.garcia-diaz@srnl.doe.gov
Business Contact:	Matt Biasiny, Contract Administration Phone: (803) 952-8648 Email: Matthew.Biasiny@srs.gov
DOE Project Officer:	Joseph Stekli
DOE Tech Manager:	Levi Irwin

Executive Summary

The objective of this project is to increase Concentrated Solar Power (CSP) system lifetime through characterization of corrosion mechanisms in heat transfer systems and identification of materials and corrosion resistance methods applicable at temperatures above 850°C. Coupling of experimental methods with thermodynamic and kinetic modeling has given greater insight into the corrosion phenomena and enabled modeling of the corrosion in molten chloride heat transfer systems. The project has been identified the selective oxidation of Cr along the grain boundaries of high Cr content alloys as the principle corrosion mechanisms occurring in CSP systems. The corrosion rate was also found to be mass transfer limited by diffusion of chromium chlorides along the grain boundaries. It was shown that the corrosion could be increased by adding naturally convective flow to mechanism using a thermosiphon.

A reaction mechanism has been proposed for selective oxidation of Cr that is driven by the electrochemical potential difference between the Ni crucible for immersion testing and the alloy coupon. This driving force will be similar to the differences caused by having varying Ni content or Cr content throughout a heat transfer system. It could also mimic the differences in electrochemical potential between various parts of the system that are at different temperatures. The reaction mechanism consists of an initiation step due to system impurities and a set of propagation steps that results in formation of a NiCr alloy at the crucible that drives corrosion and selective oxidation of Cr from the alloy. The presences of chromium chlorides in the salt are also essential to the corrosion mechanism to transport the Cr. The formation of a NiCr alloy on the crucible surface with no contact between the alloy coupons and the crucible provides support to this mechanism of having corrosion reactions occurring at both the alloy and the crucible. The thermodynamics of this reaction mechanism have been modeled and were shown to be galvanic.

A corrosion model has been developed based on this mechanism and has been implemented in CFD so that it can be used to predict corrosion in a wide variety of system geometries. The model was validated using the thermosiphon data and dimensionless analysis. The corrosion rates of the samples were modeled to within 10% percent of the experimental values. The model has been extended to include the effect of Mg corrosion inhibitor on the corrosion rate in the system.

The use of Mg as a metallic corrosion inhibitor has been demonstrated as a method to reduce the corrosion rate of alloys in molten chlorides to below 15 microns per year. Mg is an effective corrosion inhibitor at concentrations as low as 0.3 mol%. Corrosion potential monitoring experiments have shown that the Mg lowers the corrosion potential for the alloy below the equilibrium potential for Cr oxidation and thus prevents corrosion.

Experiments have been performed on the ability of Mg to inhibit corrosion in realistic environments that include lower purity salts and welded and stressed alloys. The results have shown that for all these scenarios the corrosion can be reduced to meet the DOE targets. The electrochemical monitoring of Mg for process control has also been demonstrated.

Table of Contents

Year 1 and Year 2 Key Results 4
Year 3 Testing - Introduction 16
Project Results and Discussion 18
Task 3.1: Isothermal Corrosion of Stressed and Welded HTF System Components in Molten Chloride HTFs with and without Mg 18
Task 3.2: Measure the Mechanical Properties of Alloys Exposed to $MgCl_2$-KCl and $MgCl_2$-KCl with Mg after Salt Exposure 23
Task 3.3: Modeling of Corrosion in Heat Transfer Systems 28
Subtask 3.3.1: Prediction of Corrosion Using Thermodynamic and Rate Based Models 28
Corrosion mechanism of Haynes 230 with Ni crucible in $MgCl_2$-KCl 28
Subtask 3.3.2: Prediction of Corrosion Using CFD Models 34
Cathodic protection model 34
Results 37
Task 3.4: Isothermal Corrosion in Commercial Purity Molten Chloride HTFs with Mg for Corrosion Control 41
Task 3.5: Application of Mg Additives to $MgCl_2$ Phase Change Thermal Energy Storage (TES) Systems 41
Subtask 3.5.2: Evaluation of Corrosion in $MgCl_2$ with Mg during Isothermal and Thermal Cycling 41
Subtask 3.5.3-4: Three Dimensional Simulations of Heat, Flow, and Corrosion Inside Thermal Energy Storage System from Argonne National Laboratory 42
Task 3.6: Corrosion Potential Monitoring for Process Control with Mg Corrosion Inhibiting Additive 45
Conclusions 48
Path Forward 50
References 51

Year 1 and Year 2 Key Results

The team led by SRNL has been investigating corrosion phenomena in molten chloride heat transfer systems for CSP plants and identifying methods to mitigate the corrosion. During the first year of the project, experimental characterization of the corrosion phenomena occurring in static molten salt systems were studied along with performing electrochemical characterizations of the corrosion. The results of these characterizations were compared against thermodynamic predictions of the corrosion products and models for the corrosion reactions. Figure 1 shows a cyclic potentiodynamic polarization (CPP) curves at 850°C in KCl-MgCl2 for Haynes 230, Haynes NS163, Incoloy 800 H, and Hastelloy N.

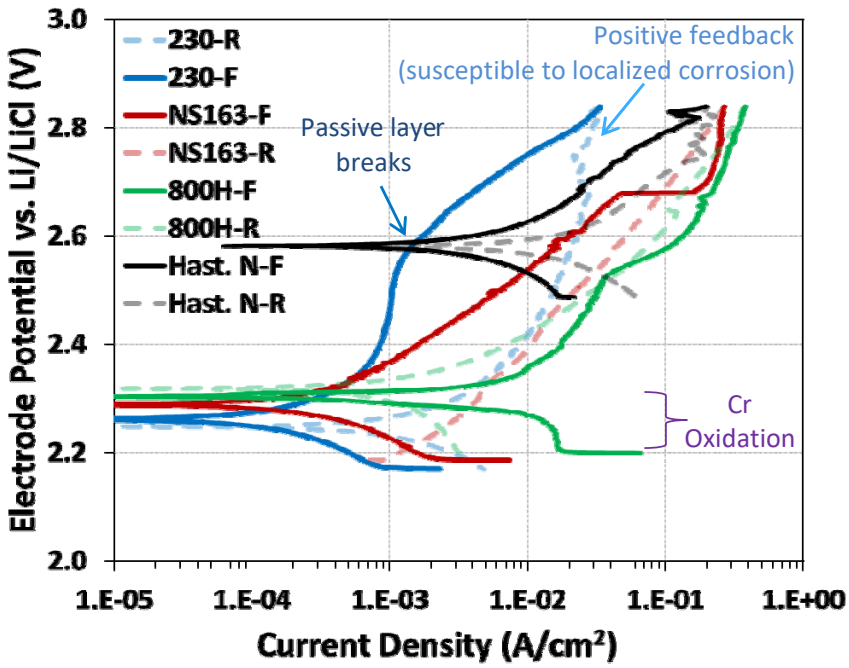

Figure 1. Cyclic potentiodynamic polarization (CPP) curves at 850°C in KCl-$MgCl_2$ for Haynes 230, Haynes NS163, Incoloy 800H, and Hastelloy N

This result illustrates several important features about corrosion of Fe-Ni-Cr alloys in molten chlorides: 1) the corrosion potentials for alloys with Cr contents above 22 wt% are all near the Cr equilibrium potential, 2) low Cr content alloys like Hastelloy N have a higher corrosion potential that is closer to the Ni equilibrium potential, and 3) the corrosion exhibits positive hysteresis and indicates localized corrosion for all cases except for Incoloy 800H where general corrosion is very high. These electrochemical results were coupled with analysis of the coupons from immersion tests to better understand the corrosion phenomena that occur. Immersion testing of Haynes 230 coupons showed that they had the lowest corrosion rate of any alloy that had sufficient strength for operation at extended times above 700°C. However, even for Haynes 230, the corrosion rate was 500 microns/yr and was more than 35 times the DOE target of 15

microns / yr. Figure 2 shows an EDS mapping overlay for Cr and Nickel for a Haynes 230 coupon at 850°C in KCl-$MgCl_2$.

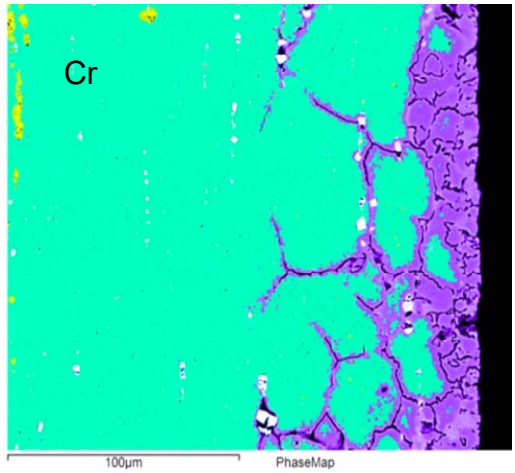

Figure 2. EDS mapping overlay of Cr (green) on Ni (purple) for Haynes 230 in KCl-$MgCl_2$ at 850°C with no corrosion inhibition.

By combining the insights from electrochemical testing in Figure 1 and the post-immersion sample analysis shown in Figure 2, it is evident that Cr is being selectively oxidized from the sample and that this selective oxidation is localized along the grain boundaries. Mn was also selectively oxidized from the alloys, but due to the low wt% of Mn in the alloys, this accounted for a much smaller portion of weight loss from the alloys. These conclusions were also similar to predictions of the principle corrosion products using Gibbs energy minimization. The selective oxidation of Cr occurred most rapidly along the grain boundaries in the alloy as can be seen in Figure 2.

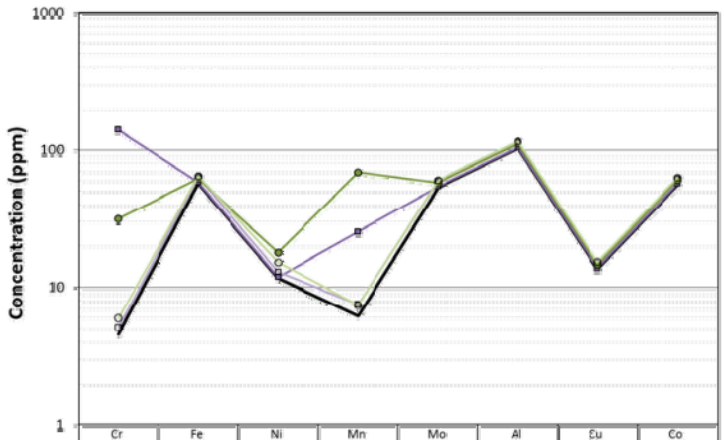

	Cr	Fe	Ni	Mn	Mo	Al	Cu	Co
MgCl2-KCl	< 4.56	< 57	< 11.6	6.17	< 53.1	< 103	< 13.5	< 55.6
NS-163	139	< 58.15	< 11.85	25.35	< 54.15	< 104.5	< 13.75	< 56.75
NS-163 + Zr	< 5.08	< 63.4	< 12.95	7.52	< 59.1	< 114	< 15	< 61.85
230	31.4	< 61.7	17.85	68.75	< 57.5	< 111	< 14.6	< 60.2
230 + Zr	5.95	< 64.5	< 15.2	7.40	< 60.1	< 116	< 15.25	< 62.9

Figure 3. Concentrations of corrosion products in molten salt after corrosion tests in KCl-$MgCl_2$ at 850°C.

Figure 3 shows the concentration of corrosion products in the salt after 100 hour immersion testing of Haynes 230 in KCl-$MgCl_2$. The corrosion products that were observed at elevated levels in the salt were Cr and Mn. These results from the salt analysis provided additional support to the theory that Cr and Mn undergo selective oxidation.

Table 1. Equilibrium potentials for electrochemical reactions calculated from thermodynamics along with concentration corrections using Gibbs energy minimization.

Haynes 230	Possible reactions	[V vs. Li/LiCl]	
		E°	E
Anodic reactions	$MnCl_2 + 2e- = Mn + 2Cl^-$	1.563	1.811
	$CrCl_3 + 3e- = Cr + 3Cl^-$	2.240	2.283
	$FeCl_2 + 2e- = Fe + 2Cl^-$	2.255	2.471
Cathodic reactions	$CrCl_3 + e^- = CrCl_2 + Cl^-$	2.730	2.691

The observed corrosion behavior of the sample with selective oxidation of Cr and Mn also fits with thermodynamic modeling of the corrosion reactions. Table 1 lists the equilibrium potentials for the main potential corrosion reactions near the corrosion potential. The main species it is anticipated could oxide based on the corrosion potential range observed in electrochemical experiments are Mn, Cr, and Fe. The main anticipated cathodic reaction is $CrCl_3$ that is produced from impurities in the system being reduced to $CrCl_2$. These corrosion reactions were combined with values of the exchange current densities and Tafel slopes of the reactions from literature and were used to construct Evans diagrams that assist in predicting corrosion rates when multiple electrochemical reactions are occurring simultaneously (mixed potential). Figure 4 shows the Evans diagram for Haynes 230 in KCl-$MgCl_2$ salt at 850°C. The corrosion rate predicted by the Evans diagrams match the experimental corrosion rate to within 10%.

The results from electrochemical testing, analysis of coupons after immersion, and analysis of the salt after testing provided significant insight about the main elements that are corroding and where the corrosion is observed. However, these results did not provide information about the rate limiting steps and the reaction mechanism. To get additional information about the rate limiting step for the corrosion mechanism, electrochemical impedance spectroscopy was performed along with immersion testing at different temperatures to get the activation energy for the reaction. Figure 5 shows results from electrochemical impedance spectroscopy (EIS) testing of Haynes 230 in $MgCl_2$-KCl at 850°C. The Nyquist diagram (left) shows that there is one main semicircle that has a line at high frequencies with a slope close to 45°. The phase angle plot at the right shows that the phase angle does not go above 45° at any frequency. Mass transfer limitations are generally known to cause a 45° feature in impedance spectra due to their distributed resistance and capacitance behavior.

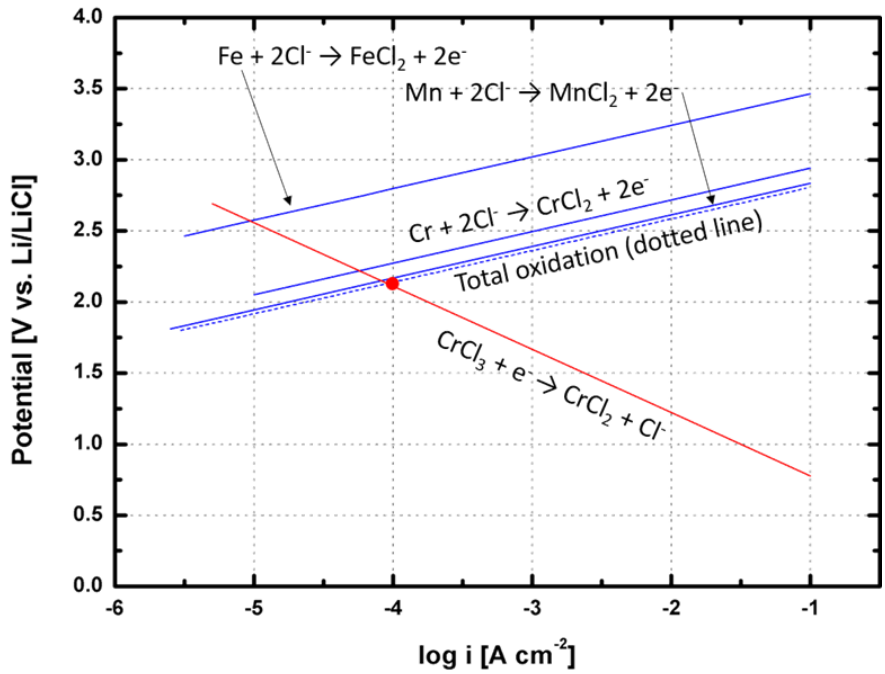

Figure 4. Evan's diagram of the corrosion reactions anticipated on Haynes 230 in KCl-$MgCl_2$ salt at 850°C.

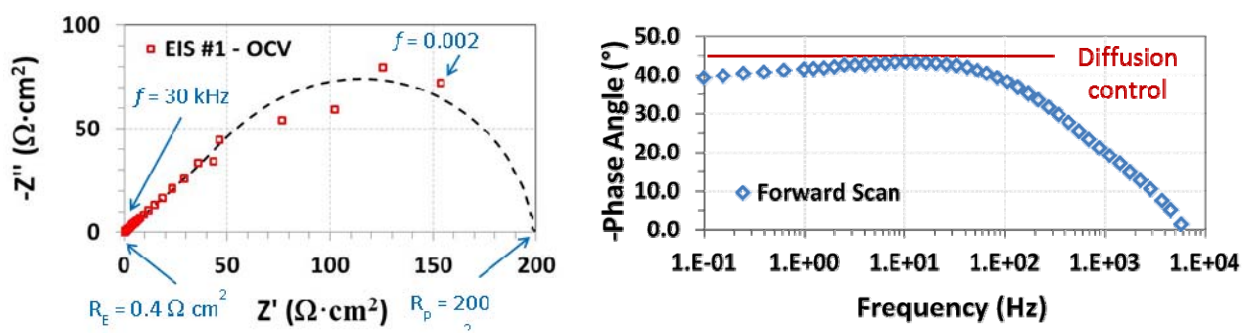

Figure 5. Electrochemical impedance spectroscopy testing of Haynes 230 at 850°C in KCl-$MgCl_2$.

Electrochemical and immersion testing was performed at different temperatures to characterize the corrosion reaction activation energy and look for additional insights into the corrosion mechanism. Figure 6 shows an Arrhenius plot of the corrosion rates measured during immersion tests at 750°C, 850°C, and 950°C. The activation energies for the corrosion reactions that were calculated from this plot were 72.7 kJ/mol for Haynes 230 and 63.5 kJ/mol for Haynes NS-163. These activation energies were compared with the activation energies for diffusion of Cr from bulk grains and diffusion of Cr along grain boundaries as shown in Table 2. The activation energies that were measured were the most similar to the activation energies for grain boundary diffusion. The similarity of the experimental activation energy to the grain boundary activation energy along with the EDS showing that the selective oxidation takes place along the

grain boundaries indicates that grain boundary this is likely the rate limiting step for the corrosion mechanism. The fact that the corrosion reaction is mass transfer limited implies that the kinetics of the corrosion reaction are faster than the mass transfer and that modeling of the corrosion reactions need to have strong consideration for mass transfer.

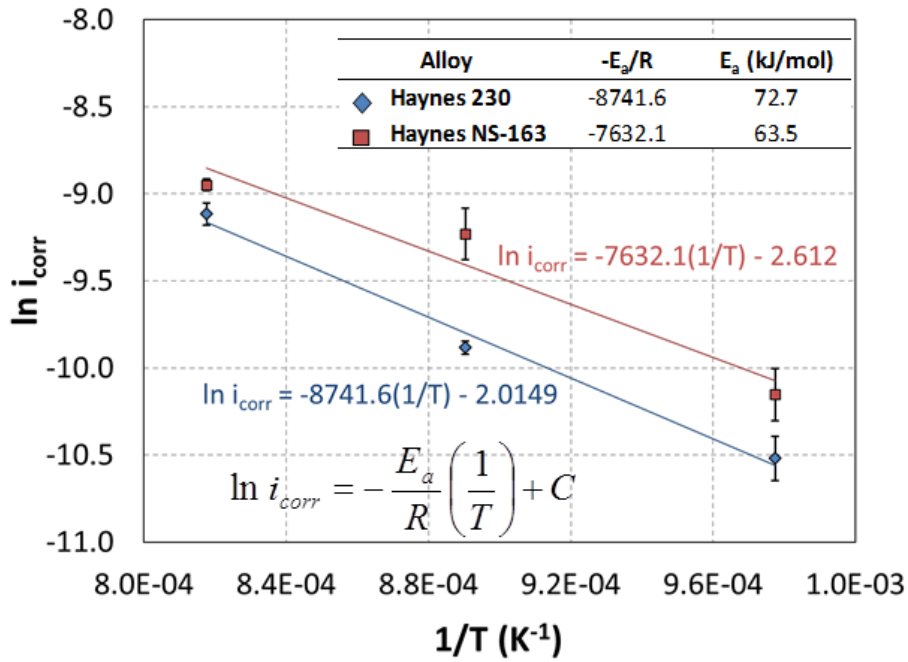

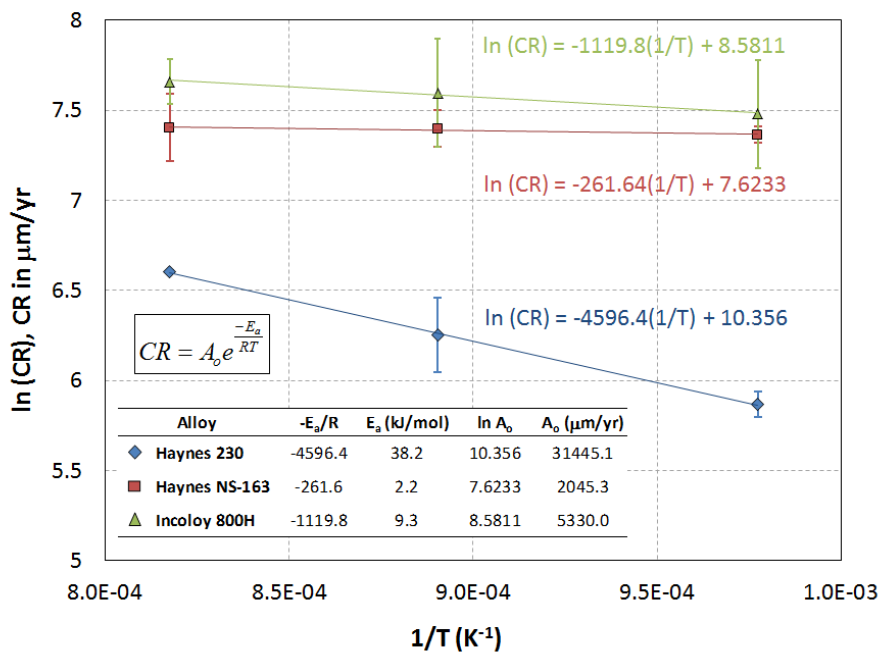

Figure 6. Arrhenius plots for Haynes 230 and Haynes NS163 in KCl-$MgCl_2$.

Table 2. Activation energy comparison between literature and experimental data.

Metal/Alloy	Temperature (°C)	Activation Energy (kJ/mol)		Reference
		Grain Boundary	Lattice	
Ni-Based Alloys	585 - 1151	150 - 350	280 - 340	Chen et al. (2003)
Ni	1100 - 1268		273	Gale (2004)
Ni (in FLiNaK)	600 - 850	120	310	Olson (2009)
SS	245 - 900	85 - 234		Mizouchi et al. (2004)
From Arrhenius Plots				
Haynes 230 (in FLiNaK)	750 - 1000	80		
Haynes NS-163 (in FLiNaK)	750 - 1000	144		
Haynes 230 (in $MgCl_2$-KCl)	750 - 950	73		
Haynes NS-163 (in $MgCl_2$-KCl)	750 - 950	64		

Olson, L. (2004), PhD. Dissertation, Univ. of Wisconsin-Madison
Gale, W.F. & Totemeier, T.C (2004), *Smithells Metals Reference Book,* 8th Ed, Elsevier.
Chen, T. et al. (2003), *Materials Transactions*, **44** (1), 40-46.
Mizouchi, M. (2004), *Materials Transactions*, **45** (10), 2945 to 2950

The immersion tests were performed in nickel crucibles because nickel does not corrode when in contact with the molten salt and because there are likely to be nickel enriched areas of the heat transfer system in molten salt heat transfer systems. In addition to analyzing the sample after corrosion, the crucibles were analyzed to understand how they are changed during the testing. Figure 7 shows an EDS line scan for Cr through the thickness of the crucible. The line scan showed that Cr was present at 7 atomic percent and decays further into the crucible. This indicates that at least part of the Cr being oxidized from the alloy is deposited into the crucible. The reduction of Cr in the salt to alloy with the nickel crucible could potentially provide a driving force to cause corrosion. This would indicate that differences in the Cr content of alloys in the system could be a potential source of additional corrosion. This deposition occurred despite the fact that there is no electrical connection between the alloy sample and the crucible. This indicates that multiple electrochemical reactions are likely occurring on the surface of the sample and the crucible to cause the corrosion and the deposition of Cr in the crucible.

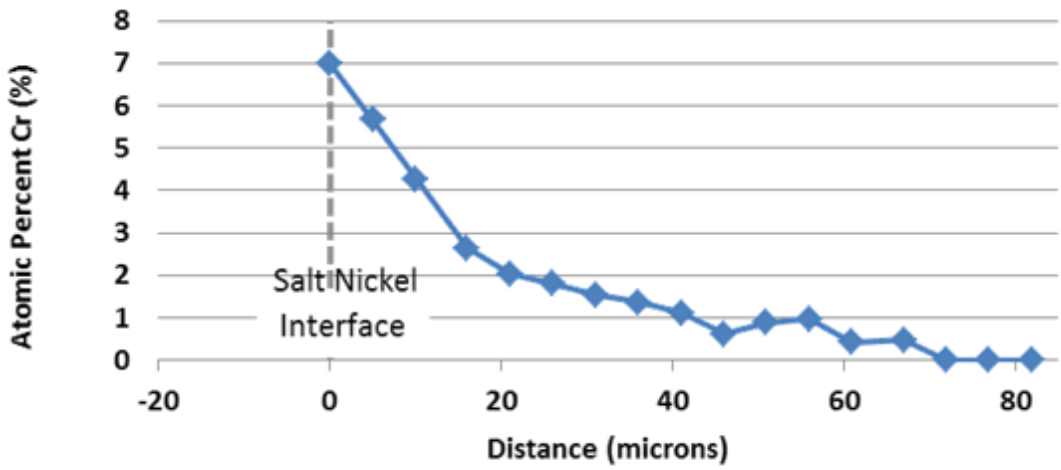

Figure 7. Cr EDS line scan of a cross-section of the nickel crucible after immersion testing of Haynes 230 in KCl-$MgCl_2$ at 850°C.

Based on the analysis of the electrochemical and immersion testing results, a reaction mechanism was developed to explain the corrosion. Figure 8 shows a proposed reaction mechanism that describes the selective oxidation of chromium in molten chloride salts. The reaction mechanism starts when some water reacts with chromium carbides that are formed at grain boundaries when the sample is heated. Although the salt is purified before testing by multistage heating, the salt is hygroscopic and there is likely some remaining moisture that could react with vulnerable carbides in the alloy to form $CrCl_3$. The $CrCl_3$ then reacts with Cr near the grain boundary to form $CrCl_2$. The $CrCl_2$ diffuses out of the grain boundaries to the bulk of the molten salt and is transported through the molten salt to the crucible. At the crucible surface, part of the chromium in the salt is reduced to form NiCr alloy and part is oxidized to form $CrCl_3$. The $CrCl_3$ is then transported back to the alloy to oxidize additional Cr. The propagation reaction cycle between the alloy and the crucible can continue until there is no differential in the electrochemical potential between the alloy and the Ni rich crucible. The occurrence of oxidation and reduction reactions on both the alloy and the crucible can explain how the alloy is corroding without having contact with crucible. Since the species in the corrosion reaction have to be transported through the bulk salt, the mass transfer coefficient of chromium chloride at the interface with the salt would have a significant impact on the corrosion rate and the concentration at the interface would change with the velocity of the fluid. This should increase the corrosion rate in the system when there is flow.

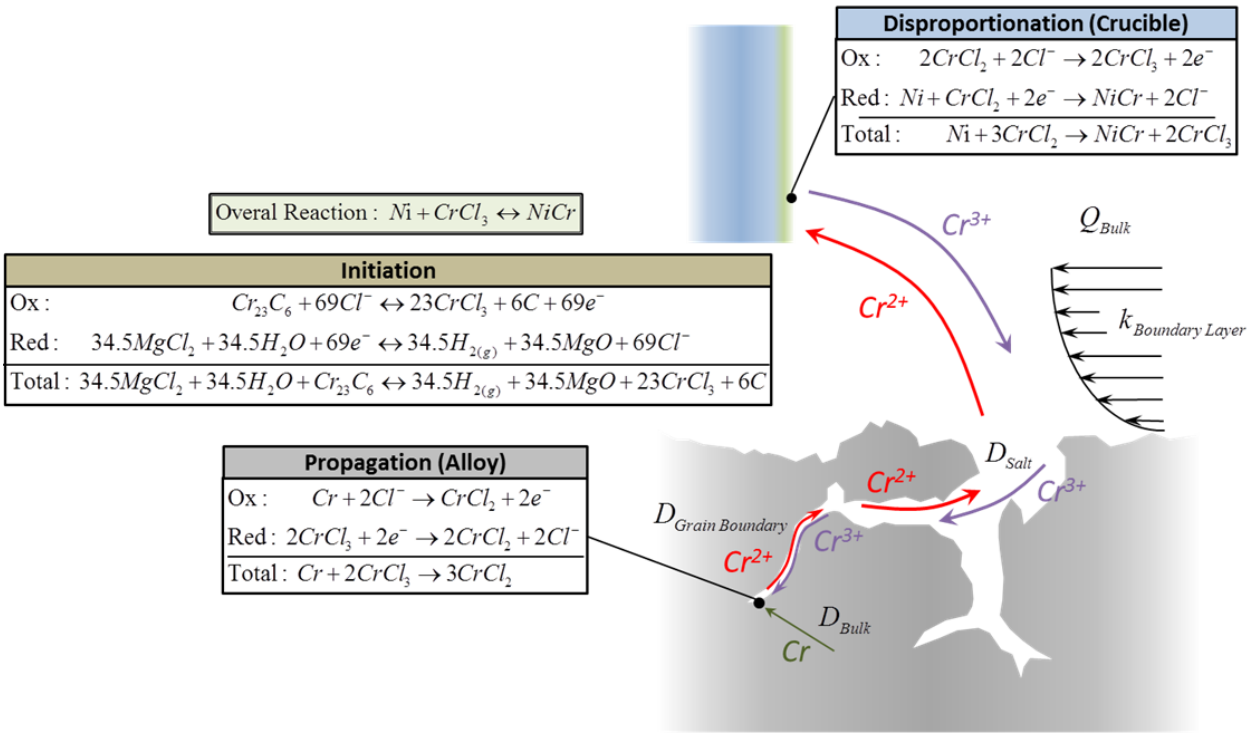

Figure 8. Proposed reaction mechanism for chromium selective oxidation.

SRNL performed experiments with a thermosiphon that added flow to the experimental system to understand how that affects the corrosion rate in the system. A diagram of the thermosiphon is shown in Figure 9. The thermosiphon creates naturally convective flow when heated from the bottom. The naturally convective mass transfer is analogous to naturally convective heat transfer and allows analysis of the flow using dimensionless correlations. For comparison with static tests, 100 hr tests were performed with an average temperature as close to 850°C as possible. A test with Haynes 230 in KCl-$MgCl_2$ showed that the corrosion rate in the thermosiphon increased to 1550 microns per year. To better understand the flow inside the thermosiphon, a computational fluid dynamics (CFD) model was made for the thermosiphon and validated against the temperature profiles in the system. Figure 10 shows the temperature profiles measured along the centerline of the thermosiphon and compares them to the profiles calculated using the CFD model. The CFD model was able to predict the temperature profiles in the thermosiphon to errors of less than 1% when compared with the experimental temperature measurements. Good agreement for the thermosiphon model was achieved for both low temperature and high temperature cases.

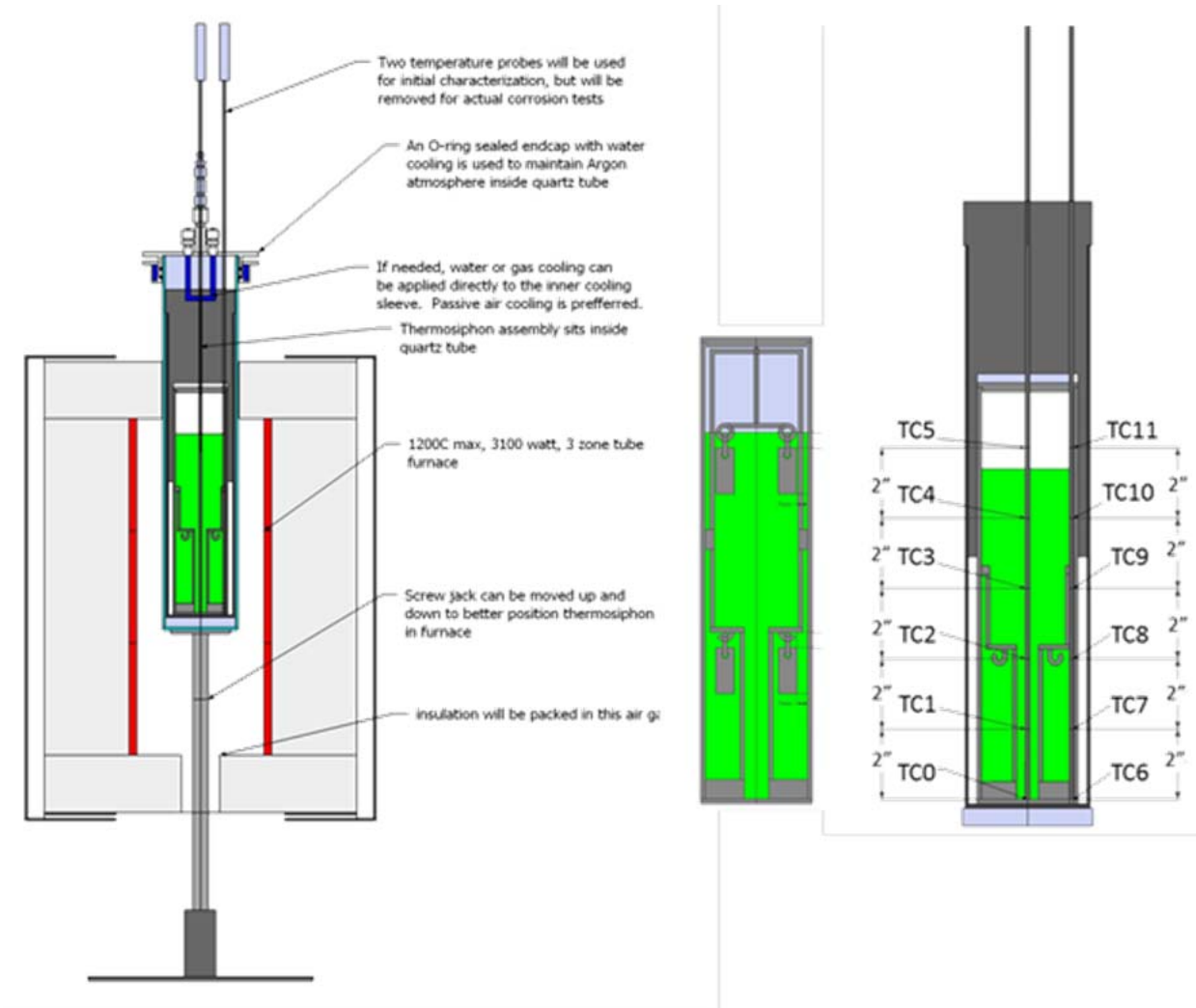

Figure 9. Thermosiphon used by SRNL to test the effect of flow on molten salt corrosion.

A corrosion model was also developed to describe the corrosion of predict corrosion rates of the isothermal static cases as well as the non-isothermal case of flow in the thermosiphon. The model for the case with flow utilized a mass transfer coefficient that was calculated using the Sherwood dimensionless number at the surface of coupons that was calculated using CFD. Figure 11 shows dimensionless engineering numbers (e.g. – Gr, Ra, Sh) calculated by CFD throughout the thermosiphon geometry. The values in Figure 11 are shown both at the edges of the geometry and in plane with the coupon. The values of the Sherwood number next to the coupon were used from the CFD simulation as inputs for the corrosion model and were used to predict corrosion rates in the thermosiphon.

The corrosion model was used to calculate the corrosion rates of static tests and thermosiphon experiments with flow. The model was able to predict all of the results to within 10% of the experimental corrosion rates as shown in Figure 12.

To mitigate the corrosion in molten chloride heat transfer systems, the use of metallic corrosion inhibitors was investigated. The goal of using metallic corrosion inhibitors is to lower the corrosion potential below the point where corrosion occurs. SRNL demonstrated that both Zr and Mg could significantly reduce or eliminate weight loss for the alloys in molten chloride systems. Zr tended to plate on the alloys and it was thought that this might be undesirable in a heat transfer system since it was unknown whether deposition would be continual over the lifetime of a CSP system. However, in some cases having an alloy coating like Zr that binds well with carbon to make stable carbides could be advantageous. Figure 13 shows the weight loss or weight gain data for runs with and without metallic corrosion inhibitors.

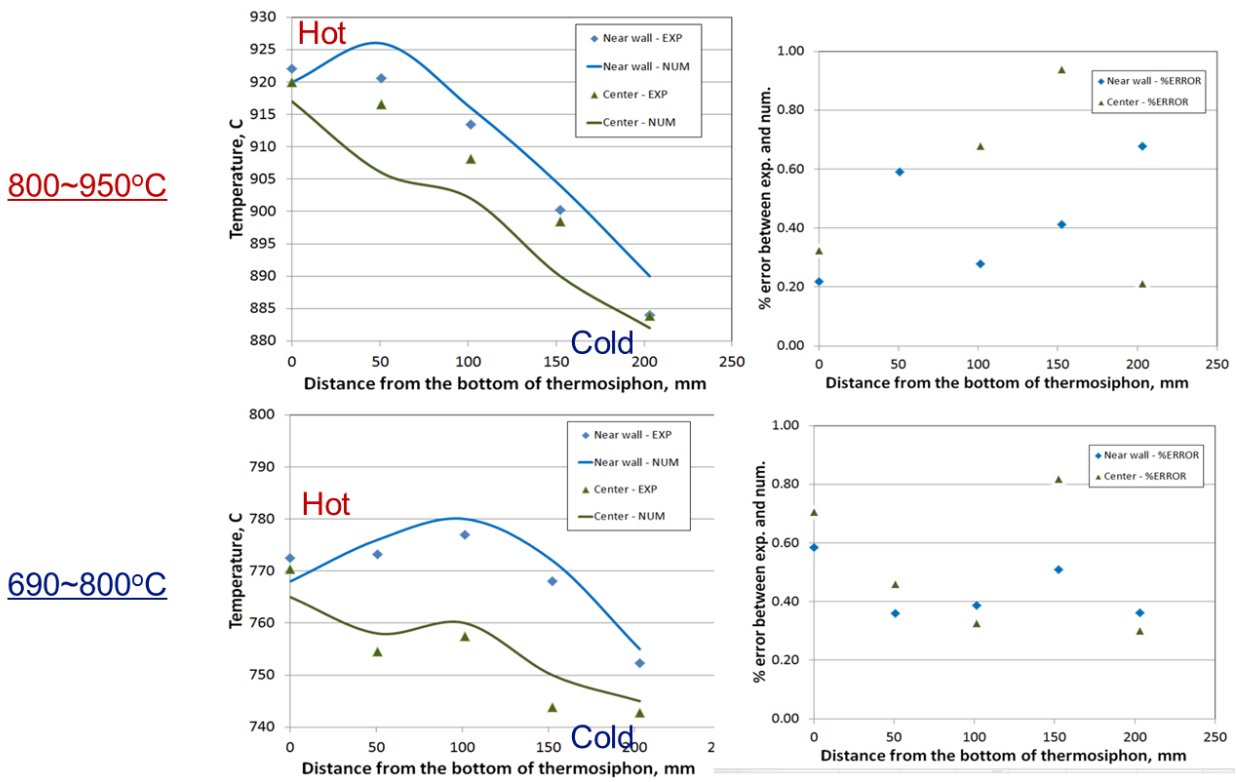

Figure 10. Validation of the CFD modeling results for the thermosiphon.

Due to the deposition of Zr that caused weight gain in the samples as shown in Figure 13, Mg was characterized in depth as a corrosion inhibitor for both the static cases and the thermosiphon. Figure 14 shows corrosion rates for Haynes 230 at 850°C in KCl-$MgCl_2$ both with and without Mg as a corrosion inhibitor for static cases and the thermosiphon. The corrosion rates with Mg for Haynes 230 are below the SunShot corrosion target of 15 microns / year. It is anticipated that the corrosion for systems with forced convection would also be inhibited given that the Mg is inhibiting the corrosion by reducing the corrosion potential below all the corrosion potentials for the constituent metals in the alloy.

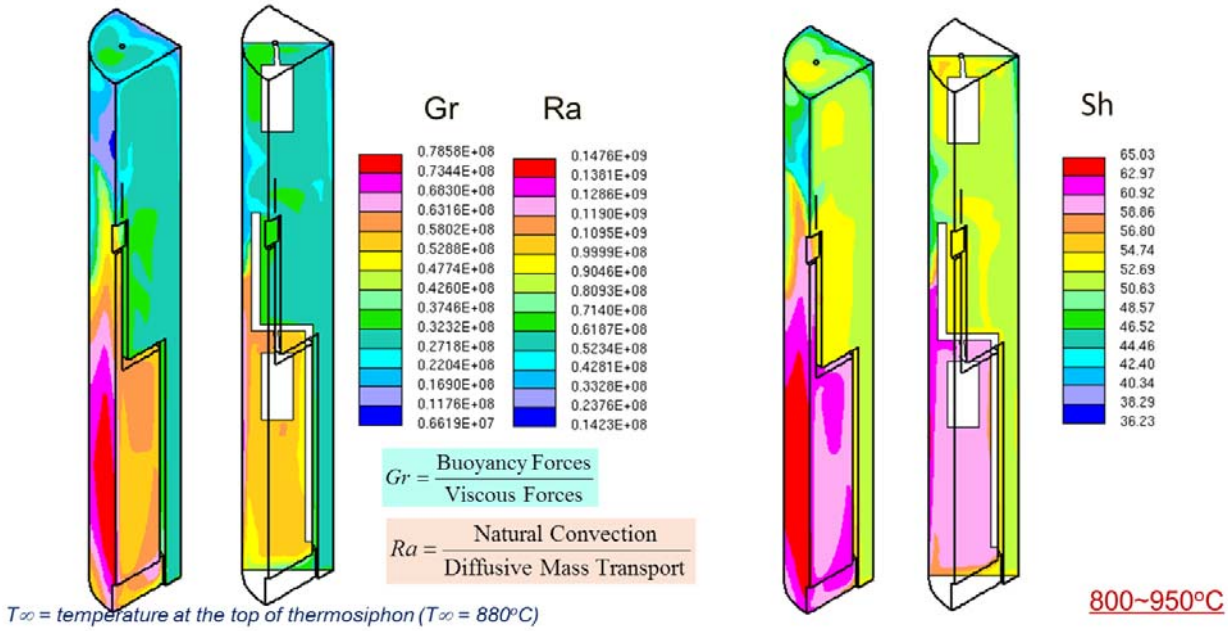

Figure 11. Dimensionless numbers in the thermosiphon calculated by CFD.

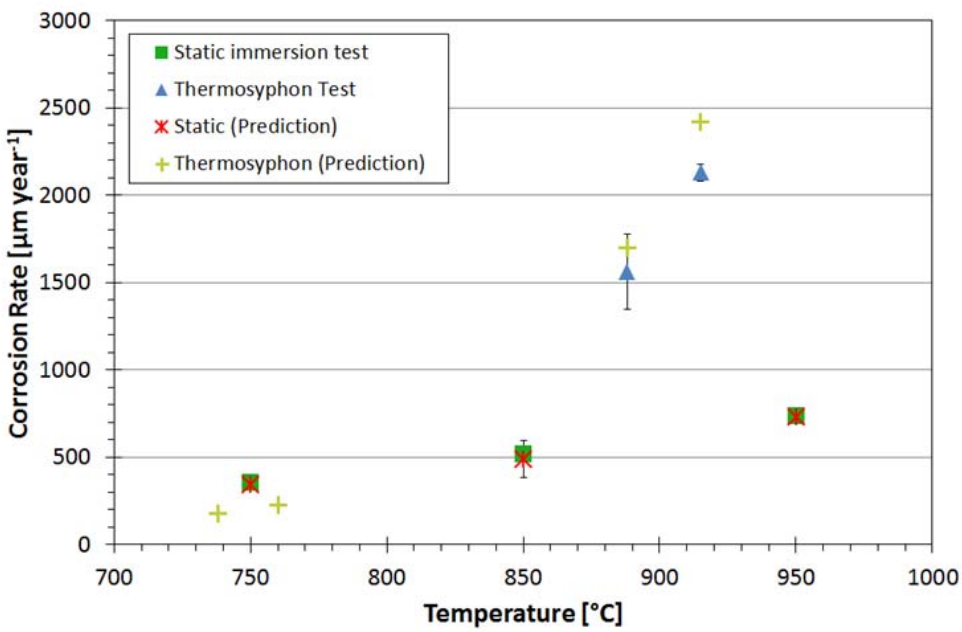

Figure 12. Comparison of model corrosion rates with experimental results.

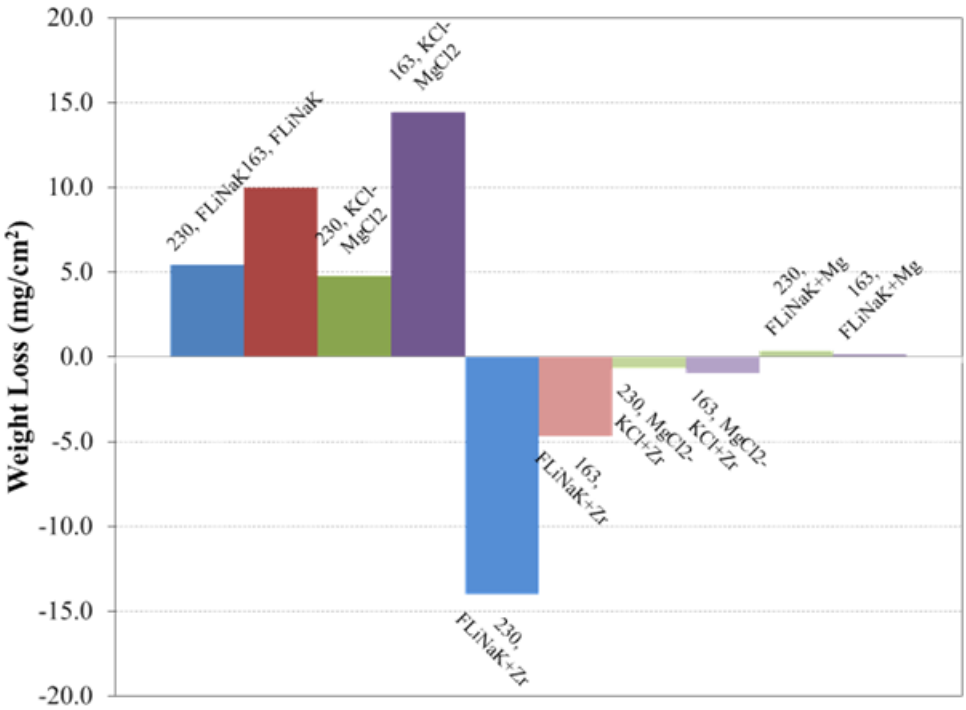

Figure 13. Weight loss or weight gain data for runs with and without metallic corrosion inhibitors.

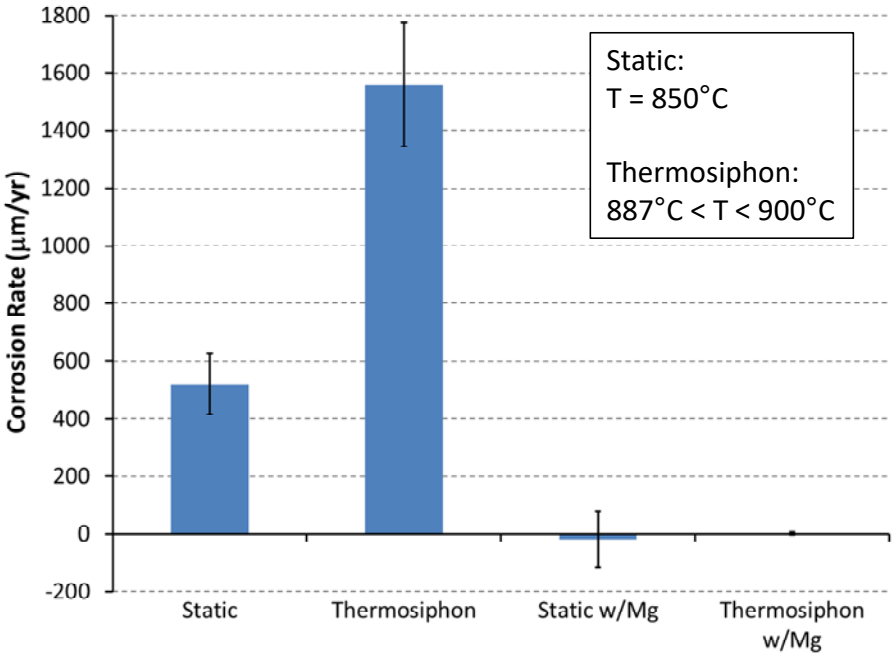

Figure 14. Effectiveness of magnesium at mitigating corrosion for Haynes 230 in KCl-$MgCl_2$ for cases with and without convective flow.

Figure 15 shows cross-sectional SEM and EDS analysis of Haynes 230 after immersion testing in KCl-$MgCl_2$ at 850°C with Mg. The EDS maps here contrast with the EDS overlay in Figure 2 for a similar run with no Mg corrosion inhibitor where the Cr was selectively oxidized. The Cr EDS map in this case shows some formation of chromium carbides that is normal when Haynes 230 is heated to high temperatures, but there is no selective oxidation of Cr. The SEM shows that the top 5-10 microns of the sample showed some rearrangement of the grains and concentration of the chromium carbides is higher just below the surface of the sample, but there was no indications that localized corrosion occurred in the presence of Mg. This shows that not only did the Mg stop weight loss in the alloy, but also stopped the specific corrosion mechanism of Cr selective oxidation along the grain boundaries. The EDS map for Mg also shows that there is no deposition of Mg in the sample when it is used as a corrosion inhibitor.

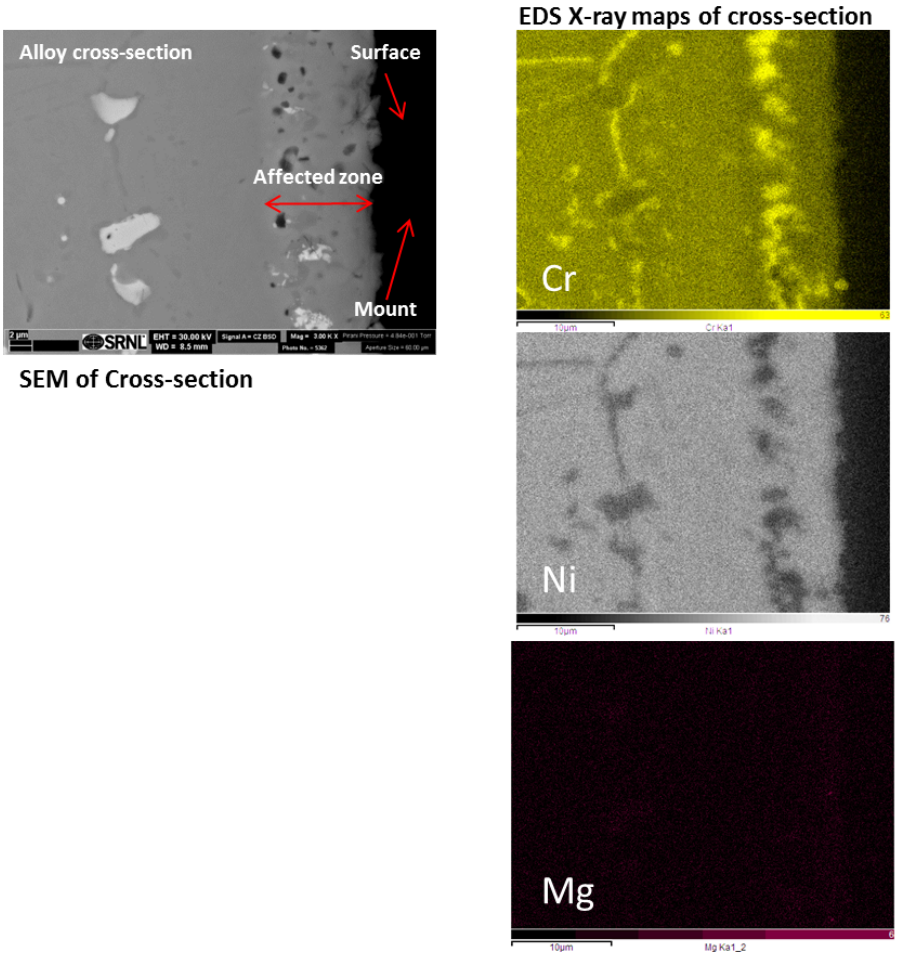

Figure 15. Cross-sectional SEM and EDS analysis of a Haynes 230 sample after immersion testing in KCl-$MgCl_2$ at 850°C for 100 hours.

Year 3 Testing - Introduction

The results from Year 1 and Year 2 in this project provided insight about the corrosion mechanism in the heat transfer alloys and showed that metallic corrosion inhibitors could be used to prevent the corrosion and bring the corrosion rate to below DOE targets. The Year 1 and Year 2 testing was performed with purified salt with flat samples that did not have any stress or welds. In Year 3, it was desired to learn more about the corrosion in realistic systems by testing with commercial purity salt along with welds and stresses. In addition, the corrosion model is being extended to include the effect of metallic corrosion inhibitors and is being applied to a phase change module (PCM) thermal energy storage system from ANL to demonstrate that the model can predict corrosion for more complex real world molten chloride systems. The milestones and completion status for this research are:

Milestone 3.1.1 - Submission of an article for publication in a peer reviewed journal. (100% Complete) – An article titled "Dimensionless Analysis for Predicting Fe-Ni-Cr Alloy Corrosion in Molten Salt Systems for Concentrated Solar Power Systems" was submitted and accepted in Corrosion Journal.

Milestone 3.1.2 – Evaluation of corrosion of stressed, welded, and welded/stressed samples. (100% Complete) – Long-term 100-hour tests in $MgCl_2$-KCl with and without Mg were performed for selected alloys that included butt welded flat, U-bended, butt welded U-bended, and fillet weld coupons.

Milestone 3.1.3 – Conclusion table with t-test comparisons. (100% Complete) – T-test comparisons of corrosion rates were reported at the 95% confidence interval for the stressed, welded and welded/stressed samples experimental matrix.

Milestone 3.2.1 – Evaluation of tensile strength of Haynes 230, Haynes NS-163, and Incoloy 800H (100% Complete) – Tensile tests have been performed for unexposed samples and samples exposed to commercial $MgCl_2$-KCl salt with and without Mg addition.

Milestone 3.3.1 – Thermodynamic simulation for mechanism of corrosion mitigation by Mg additives (100% Complete) – Thermodynamic simulations were performed to predict the corrosion potentials and corrosion mitigation by addition of mg to the molten salt

Milestone 3.3.2 – Prediction of corrosion in a thermosiphon system using CFD models. (100% Complete) – A CFD numerical model of the thermosiphon that incorporate the corrosion model has been completed. The CFD model has been used to develop a deeper understanding of the local conditions at the samples inside the thermosiphon.

Milestone 3.4.1 – Evaluation of corrosion of alloys in impure $MgCl_2$-KCl with and without Mg (100% Complete) – Long-term 100-hour tests in commercial grade $MgCl_2$-KCl salt with different Mg concentrations were performed for Haynes 230, Haynes NS-163, and Incoloy 800H.

Milestone 3.4.2 – Conclusion table with t-test comparisons. (100% Complete) – T-test comparisons of corrosion rates were reported at the 95% confidence interval for the experimental matrix in commercial grade $MgCl_2$-KCl salt and compared to the tests in pure salt.

Milestone 3.5.1 – Evaluation of changes in $MgCl_2$ heat transfer properties with addition of Mg to the salt. (100% Complete) – A combination of experiments and thermodynamic

simulations show no significant changes to melting point, density, viscosity, heat capacity and thermal conductivity of $MgCl_2$ after addition of small quantities of Mg.

Milestone 3.5.2 – Evaluation of corrosion of alloys in $MgCl_2$ with and without Mg (100% Complete) – Long-term 100-hour tests in commercial grade $MgCl_2$ salt with different Mg concentrations were performed for Incoloy 800H and temperatures.

Milestone 3.5.3 – Prediction of local electrochemical environment for the Mg/$MgCl_2$ TES system. (100% Complete) – CFD model of the TES system has been completed with the integrated corrosion model.

Milestone 3.5.4 – Development of CFD model for TES system. (100% Complete) – CFD model of the TES system has been completed with the integrated corrosion model.

Milestone 3.5.5 – Provide ANL with a salt mixture of Mg in industrial grade $MgCl_2$. (100% Complete) – A shipment of 2.5 kg of industrial grade $MgCl_2$ with Mg was delivered to ANL.

Milestone 3.5.6 – Conclusion table with t-test comparisons (100% Complete) – T-test comparisons of corrosion rates were reported at the 95% confidence interval for the experimental matrix in commercial grade $MgCl_2$ salt.

Milestone 3.6.1 – Measurements of the corrosion potential for varying Mg content. (100% Complete) – Corrosion potential monitoring were performed in commercial $MgCl_2$ with varying concentrations of Mg.

Milestone 3.6.2 – Modeling of the corrosion potential data with Mg. (100% Complete) – Electrochemical potentials have been compared with thermodynamic model containing Mg as a corrosion inhibitor. The corrosion model is able to predict corrosion rates in the presence of Mg inhibitor

Milestone 3.6.3 – Conclusion table with t-test comparisons (100% Complete) – T-test comparisons of corrosion potentials were reported at the 95% confidence interval for the experimental matrix in commercial grade $MgCl_2$-KCl salt and compered to the tests in pure salt.

Project Results and Discussion

Task 3.1: Isothermal Corrosion of Stressed and Welded HTF System Components in Molten Chloride HTFs with and without Mg

Corrosion tests of the stressed and welded samples for this task have been completed. These tests included samples for three alloys: Haynes 230, Haynes NS-163 and Incoloy 800H. Stressed and welded samples included butt welded flats, U-bends, butt welded U-bends, and fillet welded coupons. The U-bended samples were fabricated according to guidelines from ASTM G30 standard [1]. Figure 16 shows a top and front view of these welded and stressed samples for the case of Haynes 230. Figure 16(c) shows the standard flat coupon of Haynes 230 used in previous years for comparison. In addition, fillet weld coupons, as shown in Figure 17, were added to the experimental matrix after feedback from DOE. Similar samples were fabricated for Haynes NS-163 and Incoloy

800H. Also, only Haynes 230 contains corrosion tests with all the stressed coupons types.

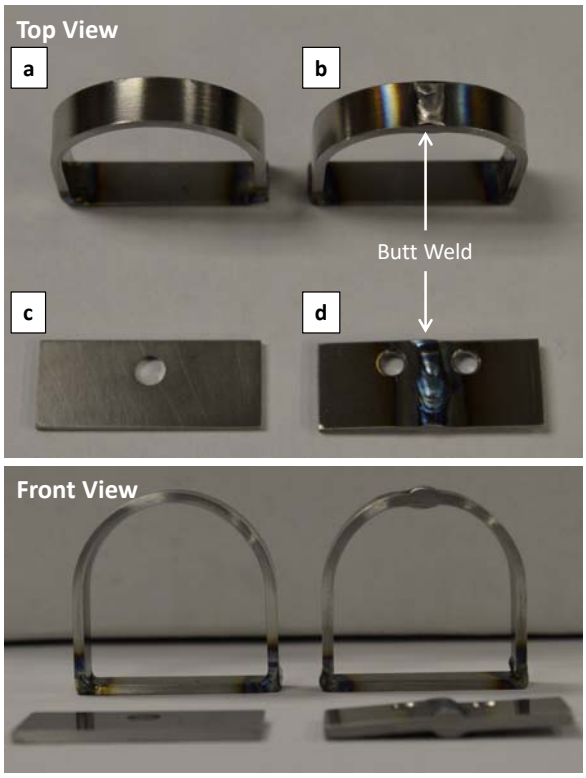

Figure 16. Haynes 230 finished samples for (a) U-bended coupon, (b) welded U-bended coupon, (c) flat coupon, and (d) welded flat coupon.

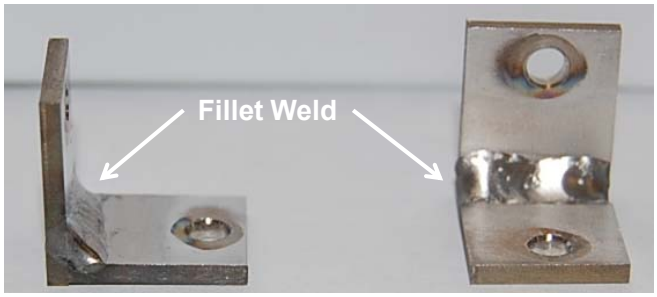

Figure 17. Two pieces of metals joined at a perpendicular angle with a fillet weld.

The isothermal corrosion tests for the selected alloys were performed in either pure salt, consisting of 99% pure $MgCl_2$ and 99% purity KCl, or commercial salt, consisting of 98% pure $MgCl_2$ and 99% purity KCl. Table 3 shows the nomenclature used to differentiate the type of stressed coupons or conditions. Salt preparation and coupons shape and dimensions have been addressed in previous quarterly reports [2].

Table 3. Nomeclature used in the corrosion rate comparison table (T-Test tables).

Abbreviation	Sample Type or Condition
Std	Standard flat coupon
W-Std	Standard flat coupon with butt weld at the center
U	U-bended coupon
W-U	U-bended coupon with butt weld at the bend section
W-L	Fillet weld coupon with joint at 90° (L-shape)
TC	Indicates under thermal cycling conditions

Table A.1 through Table A.3 in Appendix A show the average corrosion rates in the pure and commercial $MgCl_2$-KCl salts both with and without Mg addition at 850°C for Haynes 230, Haynes NS-163 and Incoloy 800H, respectively. These tables cover 100 hr static immersion tests from all project years in order to show the T-test analysis. Figure 18 to Figure 20 show plots of the corrosion rate results for the three alloys, respectively. For Haynes 230, results show that the corrosion rate varies with the type of coupon. For the standard coupon and all the alloys, the corrosion rate was similar in both pure and commercial salt. After addition of Mg to the salt, the corrosion rates of the alloys and all type of coupons met the DOE SunShot target corrosion rate of 15 μm/yr.

Species concentrations measured by ICP-OES in the post-test salt analysis are shown in Figure 21. The post-test analysis is for the 100 hr immersion tests of standard and stressed Haynes 230 coupons in commercial $MgCl_2$-KCl salt at 850°C. Concentrations for the main corroding species, Cr and Mn, are lower for tests with the stressed and welded samples.

Post-tests characterization by SEM and EDS were performed on the welds of the samples tested in commercial $MgCl_2$-KCl salt, with Mg addition, at 850°C. It is anticipated that welds at top of the U-bend samples are most susceptible to localized corrosion due to the constant imposed stress on that is highest near the weld and heat affected zone. Hence, cross-sectional SEM images of these welds, as shown in Figure 22, were examined near the weld interface. No localized corrosion is observed for Haynes 230, Haynes NS-163, or Incoloy 800H. Aside from the apparent change in secondary phase orientation from welding (stringers not aligned in Haynes 230 weld), EDS analysis of composition showed no significant differences in the metal composition from the pre-test analysis.

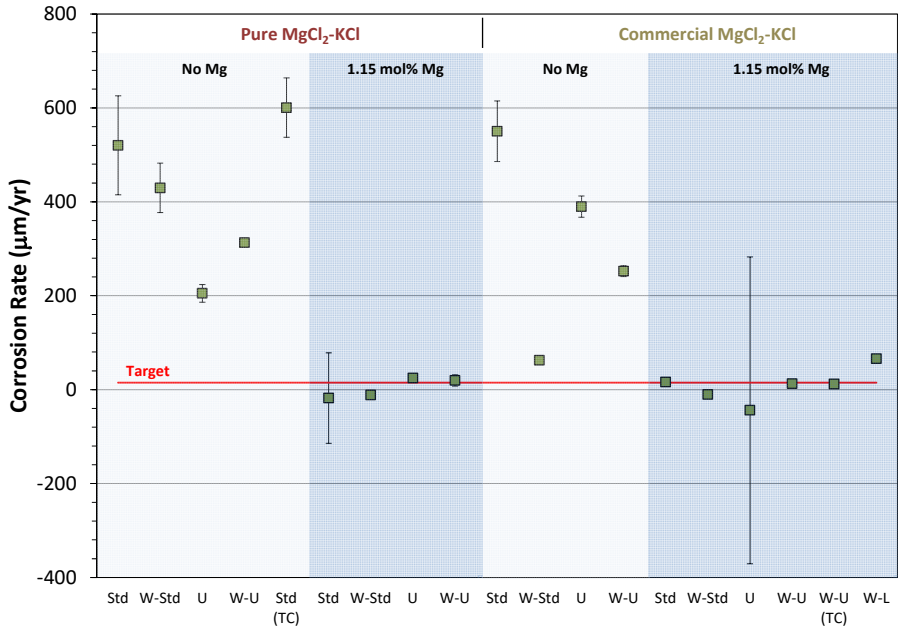

Figure 18. Corrosion rates for Haynes 230 in the pure $MgCl_2$-KCl salt, with and without Mg addition, at 850°C.

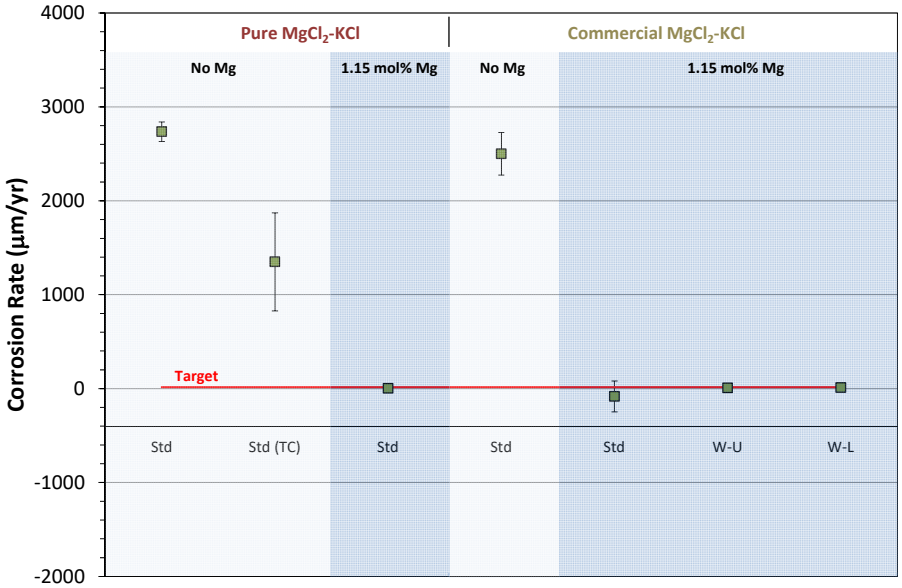

Figure 19. Corrosion rates for Haynes NS-163 in the pure $MgCl_2$-KCl salt, with and without Mg addition, at 850°C.

Figure 20. Corrosion rates for Incoloy 800H in the pure $MgCl_2$-KCl salt, with and without Mg addition, at 850°C.

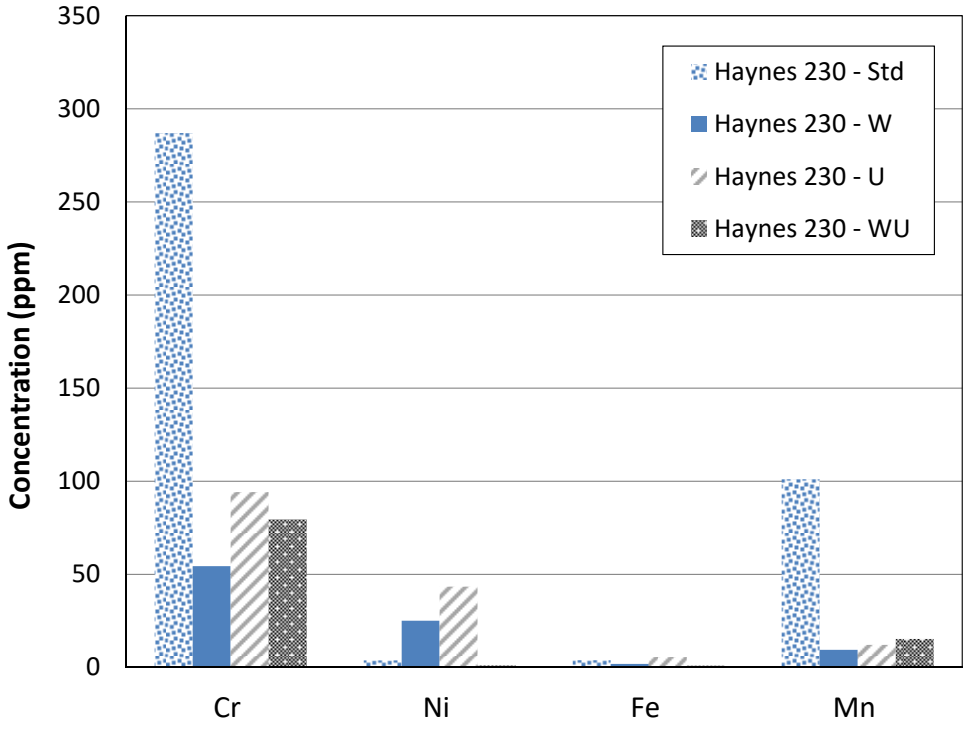

Figure 21. Post-test salt analysis by ICP-OES of 100 hrs immersion tests of standard and stressed Haynes 230 coupons in commercial $MgCl_2$-KCl salt at 850°C.

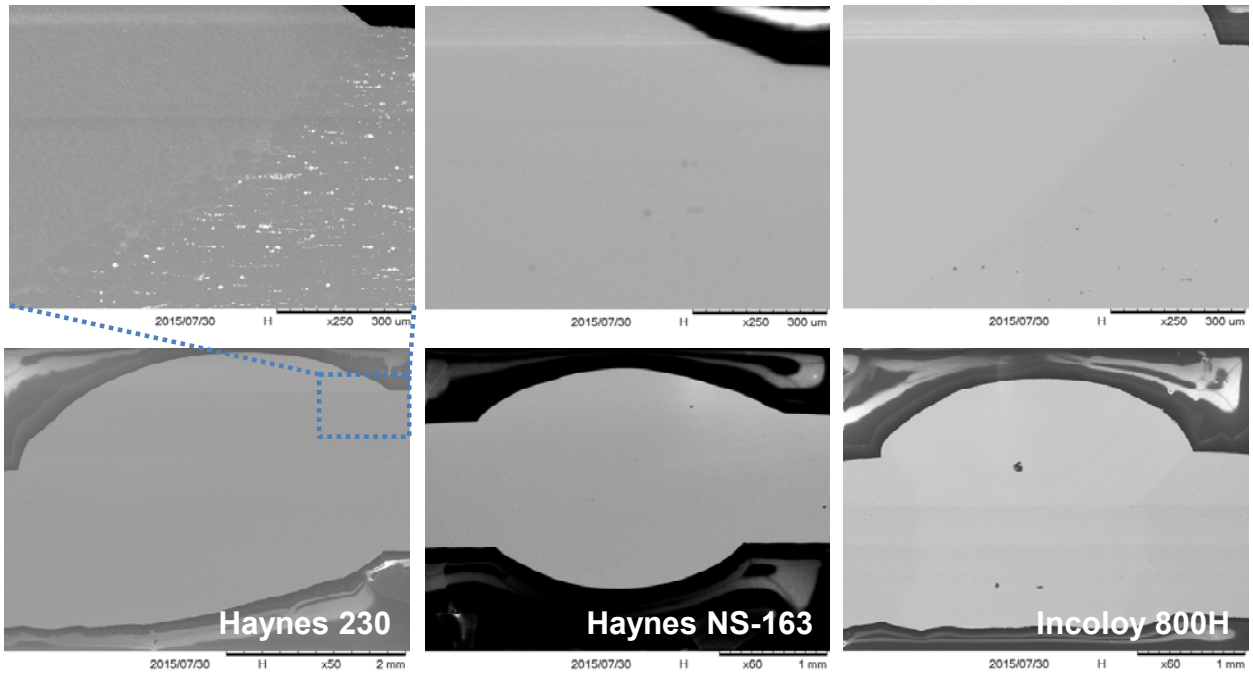

Figure 22. Cross-section SEM characterization of welds of W-U samples after 100 hrs immersion tests in commercial $MgCl_2$-KCl salts, with Mg addition, at 850°C.

Task 3.2: Measure the Mechanical Properties of Alloys Exposed to $MgCl_2$-KCl and $MgCl_2$-KCl with Mg after Salt Exposure

Corrosion immersion tests of 500 hrs for the three selected alloys were performed in commercial $MgCl_2$-KCl salt, with and without Mg addition, at 850°C. Table A.4 through Table A.6 in Appendix A show the average corrosion rate results with the statistical comparative analysis. The corrosion rate results are shown in Figure 38. The corrosion rates for Haynes 230 and Incoloy 800H from the 500 hr tests are 45% and 8% higher than the corrosion rates obtained from the 100 hr tests. However, the corrosion rate for Haynes NS-163 is 76% lower in the 500 hr test. It is possible that most of the weight loss for Haynes NS-163 occurred during the first 100 hrs of the test resulting in a lower average corrosion rate for the total period of 500 hrs. However, additional testing is needed to verify this hypothesis. Nevertheless, the addition of Mg decreased the corrosion rate for all alloys to meet the target corrosion rate.

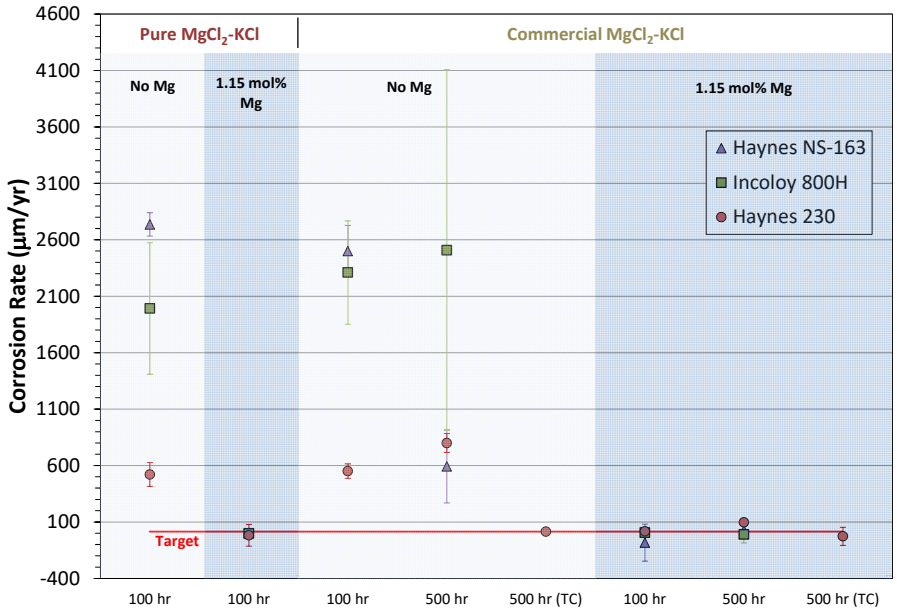

Figure 23. Corrosion rate of selected alloys from 100 hr and 500 hr immersion tests in commercial $MgCl_2$-KCl salt, with and without Mg addition, at 850°C.

Mini dog-bone shaped samples, as shown in Figure 24, were fabricated from samples of the base alloys and from samples after the 500 hrs immersion tests. Tensile tests results for Haynes 230, Haynes NS-163 and Incoloy 800H are shown in Figure 25, Figure 26 and Figure 27, respectively. A summary of the tensile tests results is shown in Figure 28. For Haynes 230, the molten salt exposure without Mg reduced the ultimate tensile strength (UTS) and elongation. However, after the addition of Mg the alloy recovered strength and some elongation. Also, results from the thermal cycling test show that the alloy recovered both tensile strength and elongation. For the case of Haynes NS-163 there is a large reduction in elongation but it has an increase of tensile strength after Mg addition. Incoloy 800H shows reduction in UTS after salt exposure with or without Mg. Also, it shows reduction in yield strength (YS) and slightly recovery of elongation with the addition of Mg.

Figure 29 SEM images were obtained for the selected alloys after fracture. Results from fractographs show small sized micro-voids in Haynes 230 after salt exposure and micro-void coalescence corresponding to cleavage or quasi-cleavage fracture from the salt exposure with Mg. Haynes NS-163 exhibited mixed mode fracture (intergranular and ductile rupture) after salt exposure but exclusively intergranular fracture surface from the salt exposure with Mg. Incoloy 800H showed mixed mode fracture surface.

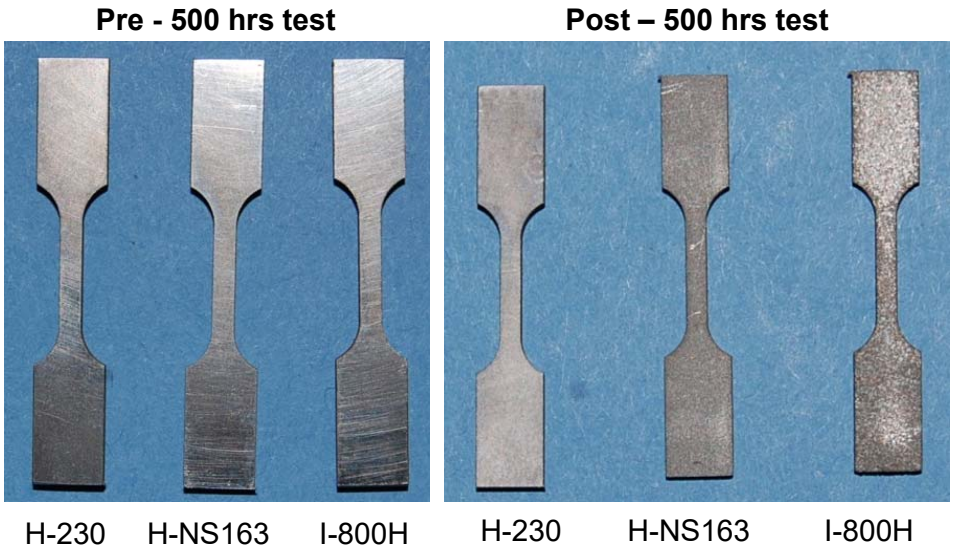

Figure 24. Specimens for tensile tests (mini dog-bone samples) fabricated from samples of the base alloys (no salt exposure) and from samples exposed to 500 hrs to MgCl2-KCl at 850°C.

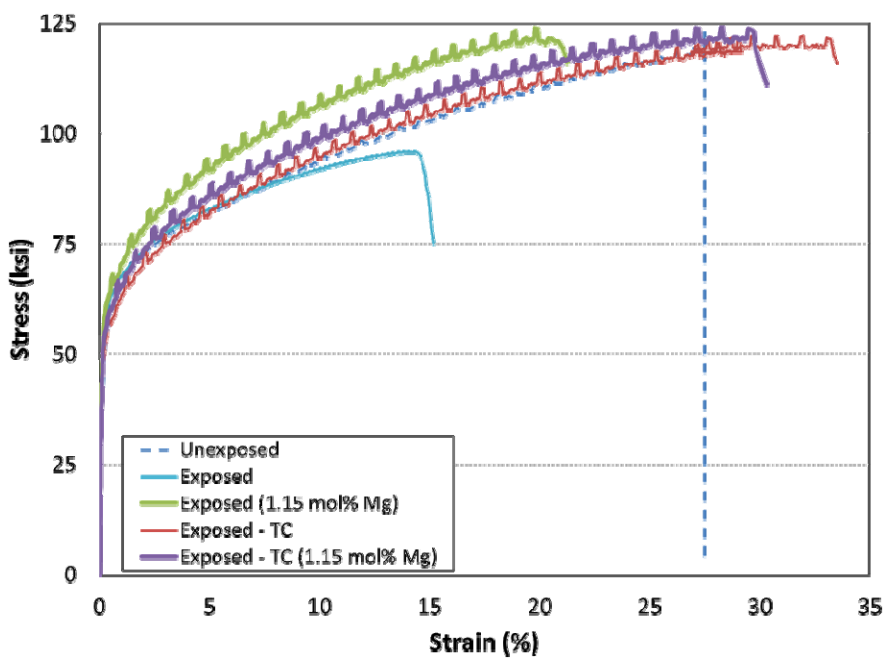

Figure 25. Tensile test of Haynes 230 of unexposed and exposed samples to 500 hrs in commercial $MgCl_2$-KCl salt, with and without Mg addition, at 850°C.

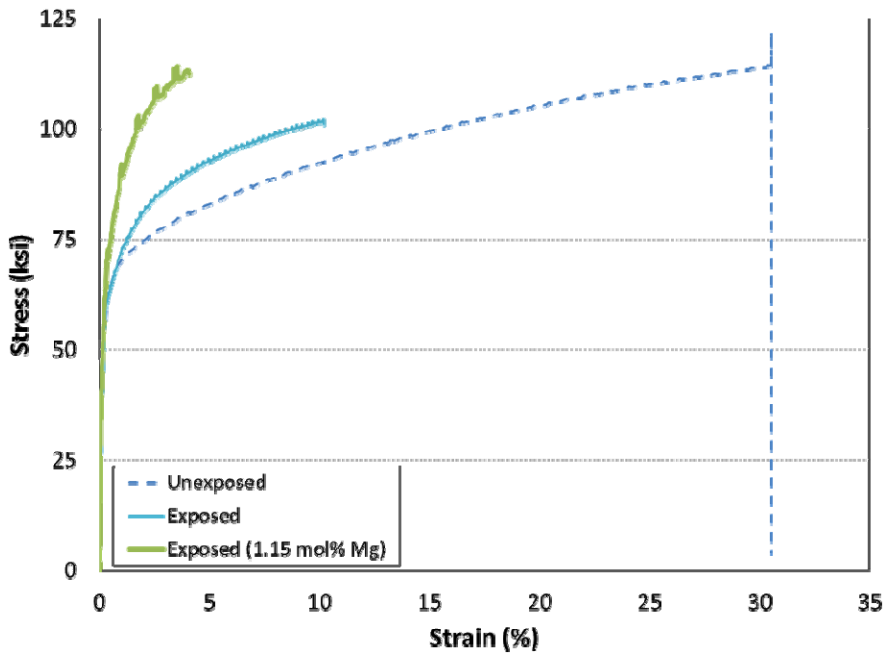

Figure 26. Tensile test of Haynes NS-163 of unexposed and exposed samples to 500 hrs in commercial $MgCl_2$-KCl salt, with and without Mg addition, at 850°C.

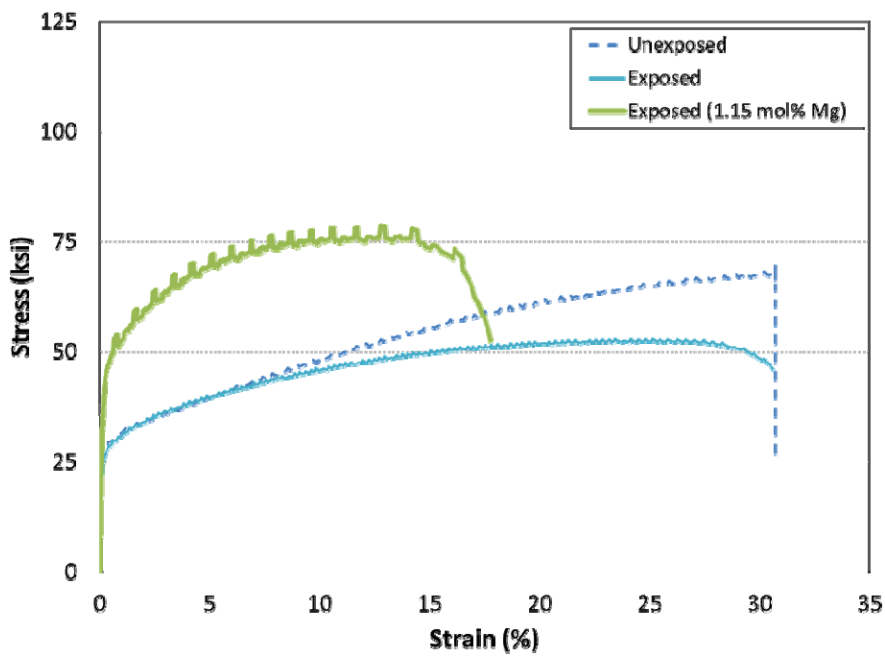

Figure 27. Tensile test of Incoloy 800-H of unexposed and exposed samples to 500 hrs in commercial $MgCl_2$-KCl salt, with and without Mg addition, at 850°C.

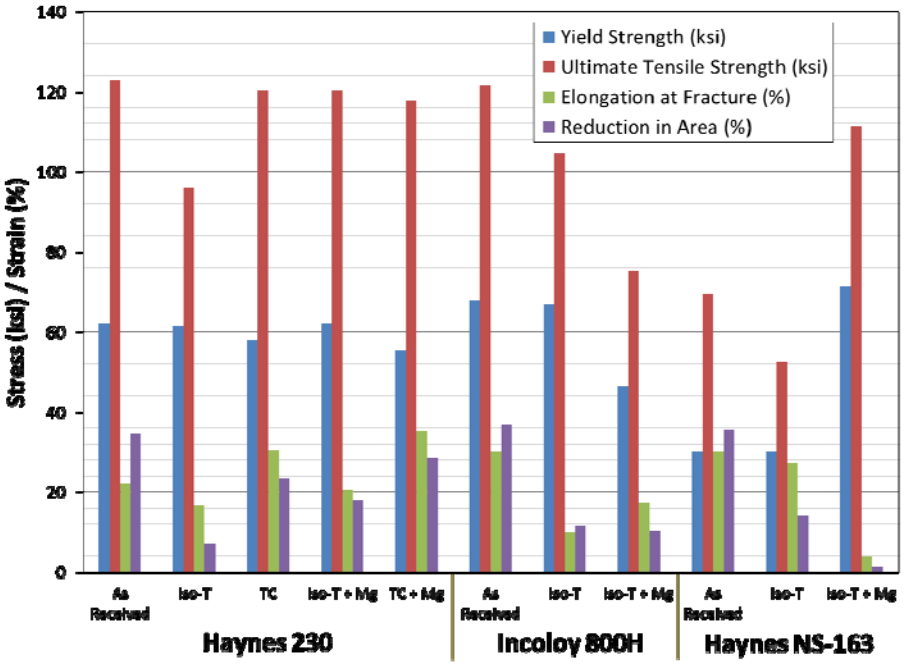

Figure 28. Summary of tensile test results for the unexposed and exposed samples to 500 hrs in commercial $MgCl_2$-KCl salt, with and without Mg addition, at 850°C.

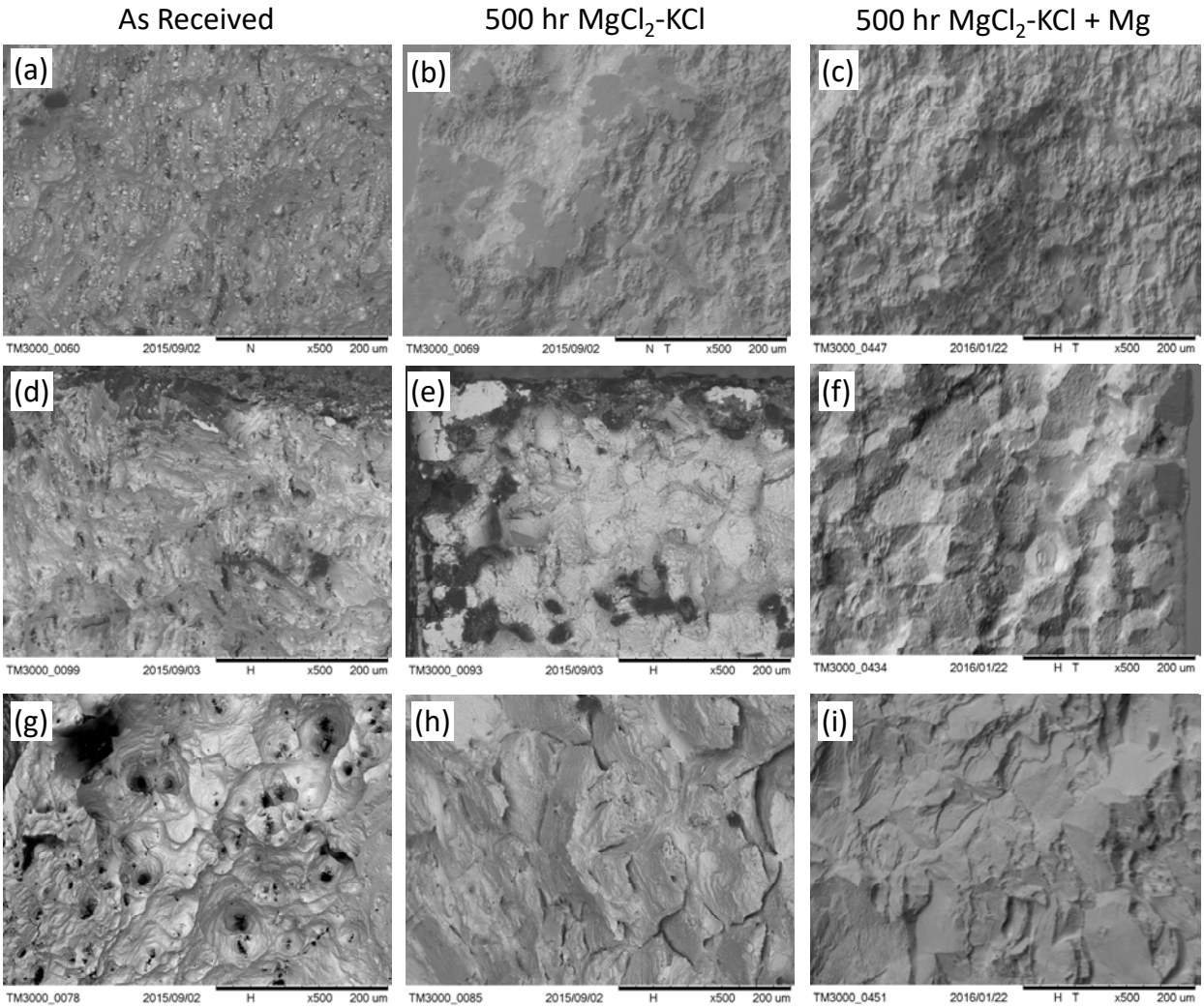

Figure 29. Fractographs for Haynes 230 (a-c), Haynes NS-163 (d-f) and Incoloy 800H (g-i) from the unexposed (as received) and exposed samples to 500 hrs in $MgCl_2$-KCl with and without Mg.

Task 3.3: Modeling of Corrosion in Heat Transfer Systems

Subtask 3.3.1: Prediction of Corrosion Using Thermodynamic and Rate Based Models

<u>Corrosion mechanism of Haynes 230 with Ni crucible in $MgCl_2$-KCl</u>

Intrinsic corrosion of Haynes 230 in $MgCl_2$-KCl has been experimentally measured. But no detailed mechanism has been reported on the intrinsic corrosion. Also, the type of the container, like Ni or graphite crucible, may also accelerate the rate of galvanic corrosion. Cr deposits on the surface of crucible and forms an alloy with the Ni or C [3, 4] The negative Gibbs energy is the driving force of the process of alloying. Cr^{3+} is more stable in fluoride salt [5] and therefore, it is safe to assume that Cr^{3+} is formed by

oxidation of the alloy, diffuses through the chloride salt and deposits the Ni crucible. Thus, the overall redox reactions are listed in (1) and (2)

$$\mathrm{Cr} \rightarrow + \mathrm{Cr}^{2+} + 2\mathrm{e}^{-} \tag{1}$$

$$Cr^{2+} + \frac{x}{y} Ni + 2e^{-} \rightarrow \frac{1}{y} Ni_x Cr_y \tag{2}$$

A. Thermodynamic Calculation of Ni-Cr Alloys

1. Gibbs energy of Ni_xCr_y alloys

As Cr is deposited on the surface of Ni crucible and with no other reactions taken place, the driving force of the depletion of Cr in the alloy is the Gibbs energy of Cr alloying with Ni. Thus, it is very crucial to know the Gibbs energy of Ni_xCr_y.

The molar Gibbs energy of Ni-Cr solution is predicted using the Equations (3)-(6) [5].

$$G_m^s = x_{Ni} G_{Ni}^s + x_{Cr} G_{Cr}^s + RT ln(x_{Ni} ln x_{Ni} + x_{Cr} ln x_{Cr}) + \Delta^{ex} G_m^s \tag{3}$$

$$\Delta^{ex} G_m^s = x_{Cr} x_{Ni} \varepsilon_{fcc} \; or \; \Delta^{ex} G_m^s = x_{Cr} x_{Ni} \; \varepsilon_{bcc} \tag{4}$$

$$\varepsilon_{fcc} = 33080 - 16.0362T \;\; Joules \tag{5}$$

$$\varepsilon_{bcc} = 34418 - 11.8577T \; Joules \tag{6}$$

where *x* is mole-fraction of element (Cr or Ni), *R* the gas constant, and *T* temperature. The quantitiesΔG_i^s, molar Gibbs energies of solution or element *i* with the s structure (liquid, bcc or fcc) in the non-magnetic state. $\Delta^{ex} G_m^s$ is the excess molar Gibbs energy. $\varepsilon_{fcc/bcc}$ is the binary interaction parameter. Because the excess Gibbs energy depends on the amount of fcc and bcc phases in the system, the quantity of each phase present is needed in order to calculate the Gibbs energy of Ni_xCr_y alloy. From Figure 30, the equilibrium mole fractions of Cr in fcc and bcc phases at 850°C are calculated as 0.4 and 0.97, respectively.

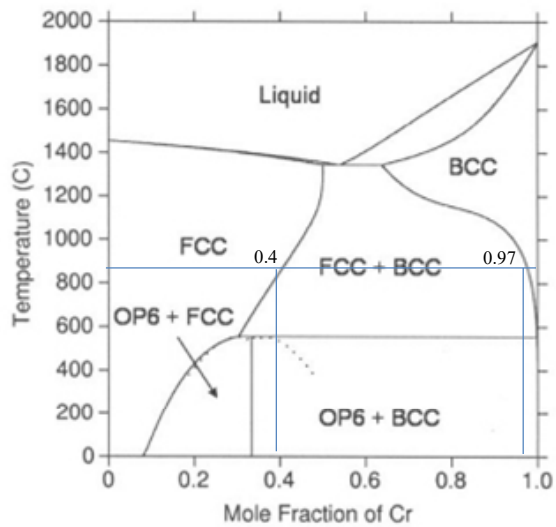

Figure 30 Phase diagram of Ni-Cr alloy [6].

Therefore, the fraction of fcc and bcc phases in the alloy can be calculated for the Cr concentration range of 0.4 to 0.97 with the lever rule shown in Equation (7).

$$\frac{x_{fcc}}{x_{bcc}} = \frac{0.97 - x_{Cr}}{x_{Cr} - 0.40} \quad (7)$$

The Equation (3) will be written as Equation (8) to calculate the Gibbs energy of Ni_xCr_y for y in the range of 0.4 to 0.97.

$$G_m^s = x_{Ni}G_{Ni}^s + x_{Cr}G_{Cr}^s + RTln(x_{Ni}lnx_{Ni} + x_{Cr}lnx_{Cr}) + x_{Ni}x_{Cr}(x_{fcc}\varepsilon_{fcc} + x_{bcc}\varepsilon_{bcc}) \quad (8)$$

As shown in the Figure 31, the molar Gibbs energy of Ni_xCr_y bcc and fcc phases are calculated from the molar Gibbs energy of Ni and Cr to be -53,582 J/mole and -43,816 J/mole at 850°C, respectively.

From Figure 31, it can be seen that the Gibbs energy of Ni_xCr_y alloy increases with increased Cr mole fraction. There is sudden change of the Gibbs energy when the Cr mole fraction is 0.4 because the bcc phase appears at this point.

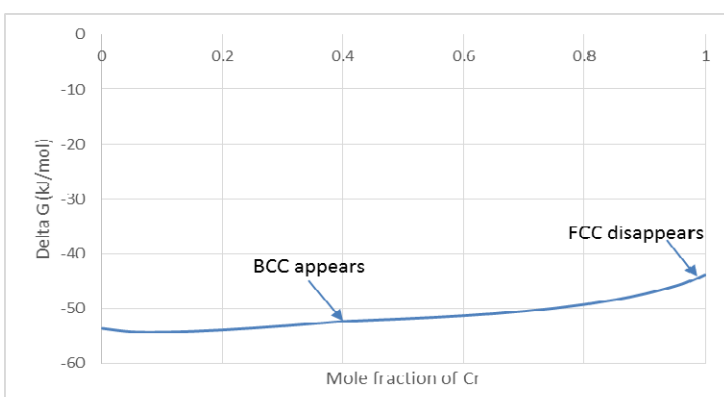

Figure 31 Molar Gibbs energy of Ni_xCr_y at 850°C.

2. Activity of Cr in Haynes 230 and Incoloy 800H alloys

The observed depletion of Cr in the salt is possibly due to the reaction of Cr with the Ni crucible, and the driving force is the Gibbs energy of the alloy formation. As expressed in the equation $\Delta G = \Delta G^{o} + RT\ln J$, the activity of Cr in the alloy must be considered in order to calculate the Gibbs energy of the reaction. Because of the presence of several elements in the alloy, the calculations are simplified by assuming that (a) the concentrations of Cr and Ni are unchanged, and (b) by considering other elements such as Fe in Haynes 230 and Fe in Incoloy 800H alloys. Therefore, the activity of Cr in Haynes 230 (0.26Cr-0.64Ni-0.10Fe) and Incoloy 800H (0.22Cr-0.29Ni-0.49Fe) versus temperature is calculated using thermodynamic modelling and the results are shown in Table 4 and Figure 30.

Table 4 Activity of Cr in Haynes 230 and Incoloy 800H at different temperatures

Temperature (K)	Activity of Cr	
	Haynes 230	Incoloy 800H
873	0.317	0.347
923	0.298	0.327
973	0.281	0.309
1023	0.267	0.291
1073	0.255	0.275
1123	0.244	0.262
1173	0.235	0.250
1223	0.227	0.239
1273	0.219	0.230

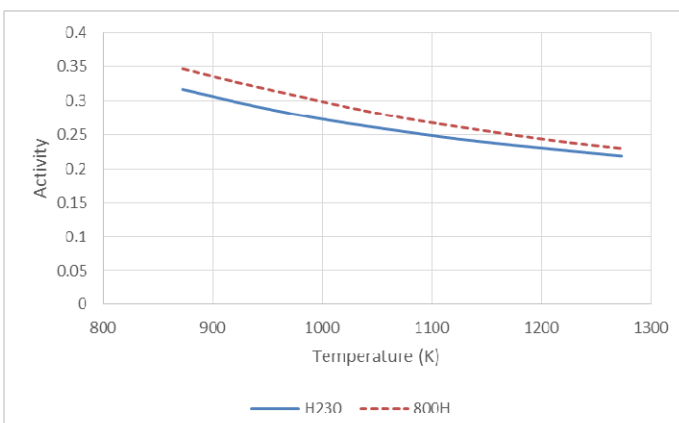

Figure 32 Activity of Cr in Haynes 230 and Incoloy 800H at different temperatures

As shown in Figure 32, the activity of Cr is decreased with the increase in the temperature for both the alloys. At 850°C, the activity of Cr in the Haynes 230 alloy is about 0.244, which is used for calculating the Gibbs energy of alloying reaction (in the next section).

3. Effect of activity of Cr in Haynes 230 on Gibbs energy of reaction

From the SRNL post-testing EDS analysis of the Ni crucible, it was observed that the concentration of Cr on the surface is about 7% after Incoloy 800H corrosion in $MgCl_2$-KCl salt. Therefore, the composition of the alloy can be estimated as $Ni_{0.93}Cr_{0.07}$. Then, the standard Gibbs energy of the Cr-Ni alloy reaction is shown in Equation (9).

$$\mathrm{Cr} + \frac{0.93}{0.07}\mathrm{Ni} = \frac{1}{0.07}Ni_{0.93}Cr_{0.07} \qquad \Delta G^{o} = -19.82\,\mathrm{kJ/mol} \tag{9}$$

As the activity of Cr in the Haynes 230 alloy is 0.244 at 850°C, the change in Gibbs energy of Cr (in Haynes 230 alloy) and Ni reaction is very negligible. Ni and $Ni_{0.93}Cr_{0.07}$ are pure solids, thus the activities are assumed to be 1. The Gibbs energy of the reaction is -7,072 J/mol. As the Gibbs energy is negative, this reaction occurs during the galvanic corrosion.

B. Corrosion Mechanism of Haynes 230 with Ni Crucible Containing $MgCl_2$-KCl Salts

1. Initiation of corrosion

At the beginning of Haynes 230 corrosion in $MgCl_2$-KCl, the corrosion mechanism is intrinsic (local) corrosion. The corrosion mechanism includes reaction with: (a) chloride salts, (b) impurities in Haynes 230 alloys (i.e. metal ions), and (c) impurities in salt (i.e. H_2O).

a. Reaction with chloride salt

Reactions with chloride salt are shown in (10) and (11):

$$\frac{3}{2}MgCl_2 + Cr \xleftrightarrow{850degC} CrCl_3 + \frac{3}{2}Mg(l) \tag{10}$$

$$3\mathrm{KCl} + \mathrm{Cr} \xleftrightarrow{850degC} CrCl_3 + 3K(g) \tag{11}$$

As the Gibbs energy of the reactions are positive, the amount of $CrCl_3$ predicted by thermodynamic modelling is very small, which is 4.44 x 10^{-14} mole $CrCl_3$ after the corrosion of 0.06 mole Haynes 230 in 169g $MgCl_2$-KCl salt.

b. Reacting with more stable metal ions

Reaction with more stable metal ion is shown in (12):

$$\mathrm{nCr} + 3\mathrm{MCl}_n = nCrCl_3 + 3M \tag{12}$$

As the Cr is more reactive than M, the Gibbs energy of this reaction is negative and the driving force may cause these reactions to occur during the corrosion.

c. Reacting with H_2O

Small amounts of $Cr_{23}C_6$ were detected at the alloy grain boundaries[7], which can easily react with chloride salt in hydrous environment. Thus, two different reactions with H_2O are possible as shown in (13) and (14):

$$34.5MgCl_2 + 34.5H_2O + Cr_{23}C_6 = 34.5H_2(g) + 34.5MgO + 6C + 23CrCl_3 \quad \Delta G = -2639.759\ kJ/mol \tag{13}$$

$$1.5MgCl_2 + 1.5H_2O + Cr = 1.5H_2(g) + 1.5MgO + CrCl_3 \quad \Delta G = -132.37\ kJ/mol \tag{14}$$

As Gibbs energies of the reactions are negative and $MgCl_2$-KCl easily absorb H_2O, this mechanism is dominant during initial corrosion and thus increase the amount of Cr^{3+} in the chloride salt.

2. Galvanic corrosion with Cr^{3+} diffusion

a. Calculation of potentials of anode and cathode reactions

The theoretical potential for the selective dissolution of elements from the alloy is calculated using Nernst equation given as Equation (15):

$$E = E^o - (RT/nF)\ InJ \tag{15}$$

where E^o is the standard potential calculated from the standard Gibbs energy data ($\Delta G^o = -nFE^o$), n is the number of electrons, F is Faraday constant, R is the gas constant, T is the temperature, J is the ratio of activity of i in oxidized state to the activity of i in reduced state. J were calculated considering $a(MC_{lx}) = 1$ and $a(Cl^-) = 1$, and for the alloy M, $a(M_{alloy,\ s})$ is activity of element in the alloy. As discussed earlier, there is about 0.266 Cr and 0.638 Ni in Haynes 230 and for simplification, it is assumed that other elements are Fe, then the calculated activity of Cr is 0.244 in Haynes 230 (Table 4).The potential of anode reaction is calculated using Equation (15). The overall reaction equations for the propogation steps in the reaction mechanism along with the potentials at 850°C are:

$$\text{Anode: Cr(bcc in H230)} + 3Cl^- = CrCl_3 + 3e^- \quad E = 5.40733V \tag{16}$$

$$\text{Cathode: } CrCl_3 + \frac{0.93}{0.07}Ni(fcc) + 3e^- = \frac{1}{0.07}Ni_{0.93}Cr_{0.07}(fcc) + 3Cl^- \quad E = -5.38435V \tag{17}$$

$$\text{Total: Cr(bcc in H230)} + \frac{0.93}{0.07}\text{Ni(fcc)} = \frac{1}{0.07}Ni_{0.93}Cr_{0.07}(fcc) \quad E = 0.02298V \tag{18}$$

The potential of cathode reaction is calculated from Gibbs energy of reaction using Equation (19):

$$E = -\frac{\Delta G}{nF} \tag{19}$$

n is the number of electrons transferred and F is Faraday's constant (96,485 C/mol)

The potential of total reaction is obtained by adding together the potential of redox reactions. Also, the potential of total reaction can be calculated using equation (19) and the Gibbs energy of reaction is predicted by using Equation (20).

$$\Delta G = \Delta G^{o} + RT\ln(J) \quad (20)$$

ΔG^{o} is obtained from Equation (9), R is gas constant, T is temperature, J is ratio of activity of product and reactant, which is calculated using activity of Cr equal to 0.244 and compounds activities are assumed to be 1.

C. Conclusions

The Gibbs energy of Ni_xCr_y alloy is calculated at 850°C. The calculated Gibbs energy of NixCry alloy is used in proposing the Cr corrosion mechanism of 230 alloy in $MgCl_2$-KCl salt with the Ni crucible as the container crucible. The Gibbs energy of Ni-Cr alloy is depended on the fraction of fcc and bcc phases but it increases with the increase in the concentration of Cr. The activities of Cr in Haynes 230 and Incoloy 800H alloys are calculated at different temperatures. As the temperature increases, the activity of Cr decreases to a small extent. Using activity of Cr in 230 alloy, the calculated Gibbs energy of the alloying reaction $Ni_{0.93}Cr_{0.07}$ is -7 kJ/mol. Because of the Gibbs energy of the reaction is negative, deposition Cr on the Ni crucible and formation alloy on the surface of the Ni crucible is favorable. This is in agreement with the experimental observation.

Subtask 3.3.2: Prediction of Corrosion Using CFD Models

Cathodic protection model

A corrosion model has been developed by using computational fluid dynamics to explain the effect of Mg as a corrosion inhibitor on corrosion rates and mechanisms. It is expected from the thermodynamic equilibrium potentials of the metals that the corrosion potential of samples in contact with Mg will have a lower corrosion potential. The polarization method is used to determine the new corrosion potential and current.

The oxidation and reduction reactions that are used as the corrosion reaction mechanism on the sample were:

Oxidation reaction:

$$Cr + 2Cl^{-} \rightarrow CrCl_2 + 2e^{-} \quad (21)$$

Reduction reaction:

$$2CrCl_3 + 2e^{-} \rightarrow 2CrCl_2 + 2Cl^{-} \quad (22)$$

By introducing the Mg corrosion inhibitor into the system, the oxidation of chromium is suppressed because the oxidation of magnesium is more thermodynamically favorable. All other metals that are more noble (higher reduction potential than Mg) will tend to stay in the metallic state until all Mg is oxidized. In addition, the Mg would reduce chromium chloride that is in the salt back to Cr in the metallic phase. Without chromium chloride in solution, the selective oxidation cannot occur. The additional electrochemical reactions that can occur with Mg in the system are:

Oxidation reaction:

$$Mg \rightarrow Mg^{2+} + 2e^- \quad (23)$$

Reduction reaction:

$$2CrCl_3 + 2e^- \rightarrow 2CrCl_2 + 2Cl^- \quad (24)$$

Before proceeding to the 3-D multi-physics model prediction, 0-D Evans diagram (Figure.1) was reconstructed by including Mg into the system for Haynes 230 in $MgCl_2$-KCl using parameters such as Tafel slopes, exchange current densities, and equilibrium potentials to describe electrochemical corrosion system virtually. The parameters are shown in Table 5. The construction of the Evans plot allows predictions and explanations of effects observed experimentally. That is, an intersection point of the total oxidation (dotted line) and reduction curves led to predict the rate of corrosion of Haynes 230 in $MgCl_2$-KCl.

Cathodic polarization of the alloy controls the kinetics of the electrode processes occurring on the metal-electrolyte interface. As shown in Figure 33, polarization of the cathode in a negative direction from the corrosion potential decreases the corrosion rate. By polarizing the system from E_{corr} to E'_{corr} with a known applied current through sacrificial anode the corrosion current density decreases from I_{corr} to I''_{corr}.

Table 5. Kinetic parameters used for the prediction of Haynes 230 corrosion in $MgCl_2$-KCl salt as inputs to the model

Electrochemical reactions	Temperature	Kinetic parameters			
	T [°C]	i_0 [A/cm^2]	A	n	β [V/decade]
$CrCl_3 + 3e^- = Cr + 3Cl^-$	750	1.9×10^{-5}	0.5	2	±0.135
$CrCl_2 + Cl^- = CrCl_3 + e^-$		8.7×10^{-7}	0.5	1	±0.406
$Mg + 2Cl^- = MgCl_2 + 2e^-$		5.5×10^{-8}	0.5	2	±0.135
$CrCl_3 + 3e^- = Cr + 3Cl^-$	850	1.9×10^{-5}	0.5	2	±0.148
$CrCl_2 + Cl^- = CrCl_3 + e^-$		1.8×10^{-6}	0.5	1	±0.445
$Mg + 2Cl^- = MgCl_2 + 2e^-$		7.5×10^{-7}	0.5	2	±0.148
$CrCl_3 + 3e^- = Cr + 3Cl^-$	950	1.9×10^{-5}	0.5	2	±0.168
$CrCl_2 + Cl^- = CrCl_3 + e^-$		2.5×10^{-5}	0.5	1	±0.505
$Mg + 2Cl^- = MgCl_2 + 2e^-$		1.5×10^{-6}	0.5	2	±0.168

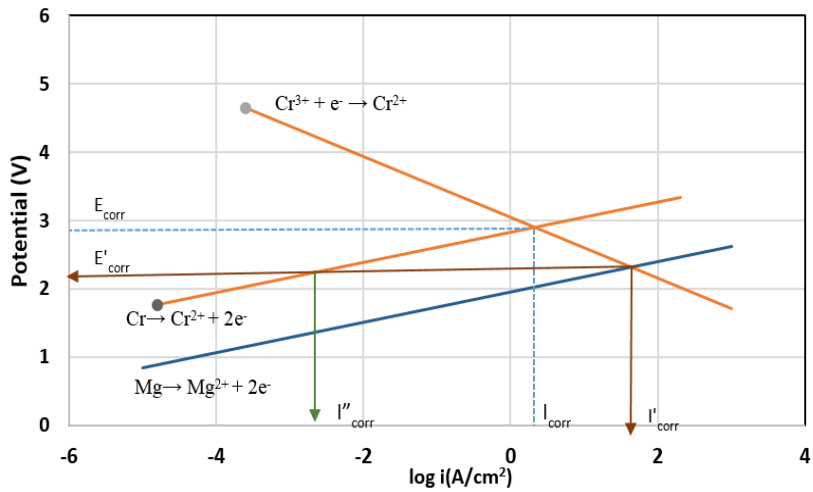

Figure 33. Evans diagram-principle of cathodic protection [8].

A single reaction (23) and (24) can be written in symbolic form as:

$$n_j e^- \leftrightarrow \sum_{i=1}^{n} s_{i,j} S^{z_i} \tag{25}$$

So for source and sink terms:

$$N_{Cr^{3+}} = \frac{-2i^c}{2F} \tag{26}$$

$$N_{Cr^{2+}} = \frac{2i^c}{2F} \tag{27}$$

$$N_{Mg^{2+}} = \frac{i^a}{2F} \tag{28}$$

$$N_{Mg} = \frac{-i^a}{2F} \tag{29}$$

According to Butler-Volmer kinetics, in the present model, kinetics of anodic and cathodic reactions can be estimated from

$$i_a = i_{0,a} \exp\left[\frac{(1-\beta)n_a F}{RT}(E^a - E_F^a)\right] \tag{30}$$

$$i_c = -i_{0,c} \exp\left[\frac{-\beta n_c F}{RT}(E^c - E_F^c)\right] \tag{31}$$

Where E_F^a and E_F^a are the anodic and cathodic equilibrium potential calculated from Equations (32) and (33). E (V) is the surface potential, β is the symmetry factor and F is the Faraday constant. $i_{0,a}$ and $i_{0,c}$ are the anodic and cathodic exchange current density and calculate from Equations (34) and (35).

$$E_E^a = E_0^a - \frac{RT}{n_a F}\ln\left(\frac{C_{Mg^{2+}}}{C_{Mg}}\right) \tag{32}$$

$$E_E^c = E_0^c - \frac{RT}{n_c F}\ln\left(\frac{C_{Cr^{2+}}}{C_{Cr^{3+}}}\right) \tag{33}$$

where E_0^a and E_0^c are the anodic and cathodic potential at standard-state conditions.

$$i_{0,c} = \frac{i_{0,c}^{ref}\, C_{Cr^{2+}}{}^{\beta}\, C_{Cr^{3+}}{}^{(1-\beta)}}{(C_{ref,Cr^{2+}})^{\beta}(C_{ref,Cr^{3+}})^{(1-\beta)}} \tag{34}$$

$$i_{0,a} = \frac{i_{0,c}^{ref}\, C_{Mg}^{\beta}\, C_{Mg^{2+}}{}^{(1-\beta)}}{(C_{ref,Mg})^{\beta}(C_{ref,Mg^{2+}})^{(1-\beta)}} \tag{35}$$

where i_0^{ref} is the exchange current density for some conventionally selected values of C_i^{ref}.

The electrochemical potential at the metal surface E (i.e., corrosion potential) or open circuit potential can be found from the current (charge) balance equation at the metal surface:

$$E^a = E^c = E'_{corr} \tag{36}$$

$$|i_c| = |i_a| = |i'_{corr}| \tag{37}$$

Cathodic protection eliminates the potential differences between the anodes and cathodes on the corroding surface. A potential difference is then created between the cathodic protection anode and the structure such that the cathodic protection anode has a more negative potential than any point on the structure surface. Thus, the structure becomes the cathode of a new corrosion cell. By polarizing the alloy surface from E_{corr} to E'_{corr} the corrosion current decreases from I_{corr} to I''_{corr}.

Results

A comparison of the prediction of local corrosion rates and corrosion potential for Haynes 230 coupons in $MgCl_2$-KCl for an isothermal case are shown in Figure 34 (a) and (b) respectively. The calculation was carried out in the temperature of 750 ℃, 850 ℃, and 950 ℃ for isothermal conditions without cathodic protection. The prediction demonstrates higher corrosion rates and corrosion potential as temperature increases and they are a good agreement between the model and the experimental data. For the case of 850 ℃ we compare the cases of with Mg and without Mg for corrosion rate as results are shown in Figure 35 the corrosion rates by model prediction with Mg and without Mg for 750 ℃ and 950 ℃ also are shown in Figure 35. A good agreement between the model prediction and the experimental results are shown for the case of 850 ℃.

The model also runs for the case with fluid flow for Haynes 230 coupons in $MgCl_2$-KCl for the operating temperature of 800-950 ℃ without Mg and with Mg. A comparison of the prediction of local corrosion rates and corrosion potential are shown in Figure 36 (a) and (b) respectively. The conditions that use in the model are shown in Table 5.

Experimental results for corrosion potential measurement for 100 hours with Mg content in the molten salt with time for different Mg concentrations, determine the dependence of the corrosion potential on the Mg concentration in the salt. The corrosion rates with varying Mg concentrations in the commercial salt against the Mg concentrations were shown in Table 6 [2] (red cells mean the experimental data is not precise enough for comparison). Table 7 is showing the comparison of Mg concentration effect on the corrosion rate for the model prediction and experimental results at 100 hours. The results of the errors also showed in the Table 7.

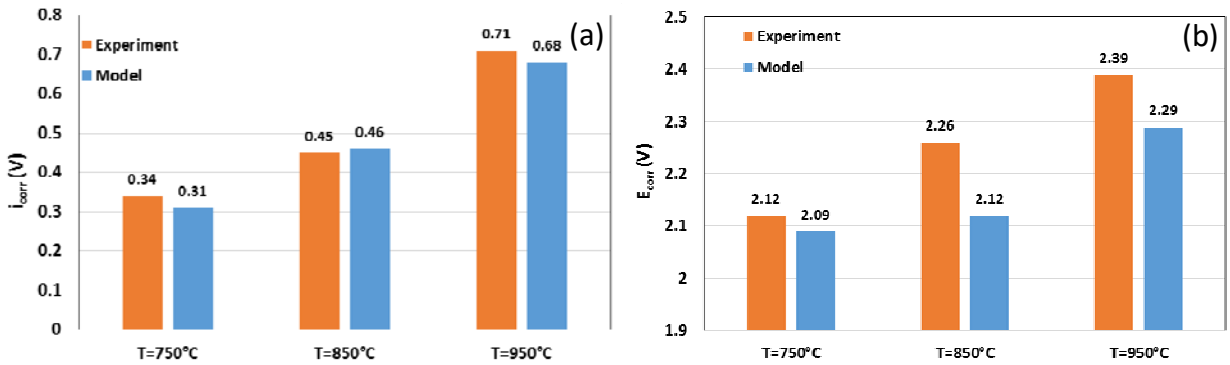

Figure 34. Comparison of corrosion rate and corrosion potential from model prediction and experimental data under static conditions at different temperatures.

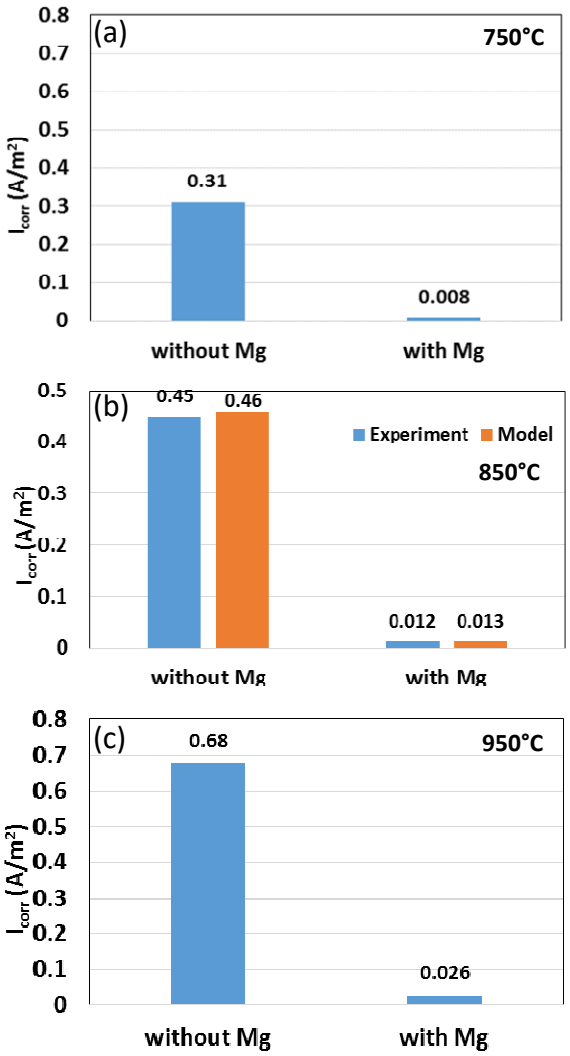

Figure 35. Comparison of corrosion rate from model prediction and experimental data under in static conditions at different temperatures with and without Mg.

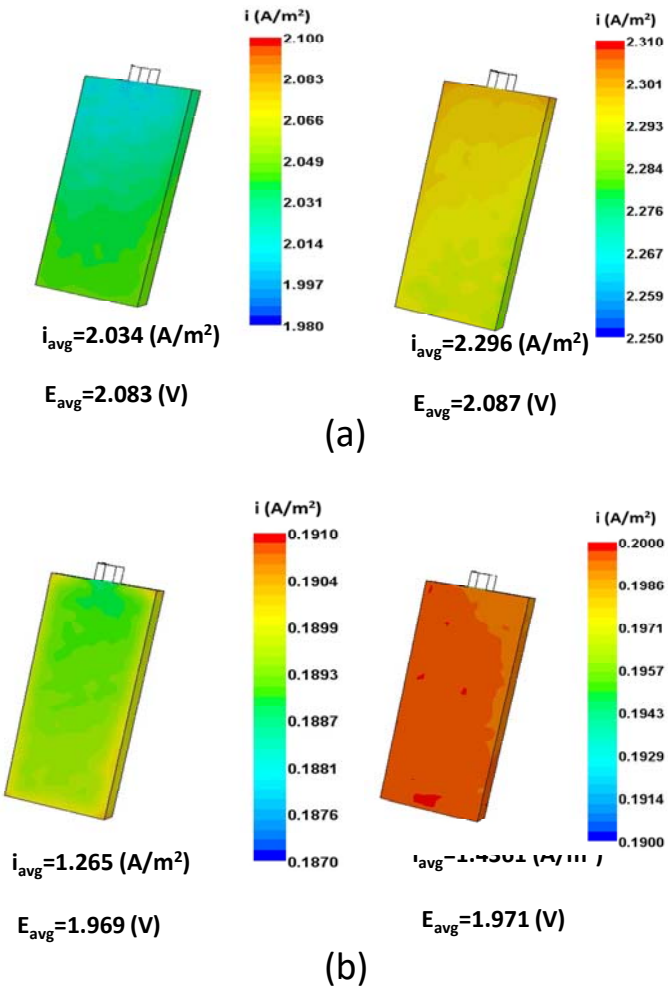

Figure 36. Corrosion rate at the surface of the coupons at cold zone and hot zone from model prediction data for the cases of without Mg (a) and with Mg (b).

Table 6. The experimental results for the effect of Mg concentration on the corrosion rate for commercial salt [1].

Mol % Mg	0	0.05	0.15	0.3	0.7*	1.15
Experimental average corrosion rate (mm/yr)	550.2 ± 64.6	468.7 ± 49	267.5 ± 22.3	65.9 ± 9.2	-------	16.3 ± 5.7

Table 7. The effect of Mg concentration on the corrosion rate.

Mol % Mg	0	0.05	0.15	0.3	0.7	1.15
Model average corrosion rate (A/cm²)	0.46	0.37	0.20	0.049	0.036	0.013
Experimental average corrosion rate (A/cm²)	0.45	0.34	0.19	0.048	---	0.012
error%	-0.6	-5.8	-1.053	-0.833	---	-5.0

Task 3.4: Isothermal Corrosion in Commercial Purity Molten Chloride HTFs with Mg for Corrosion Control

SRNL performed isothermal corrosion rate tests for the selected alloys in the commercial salt consisting of 98% pure $MgCl_2$ and 99% purity KCl. Table A.7 through Table A.9 in Appendix A show the average corrosion rate results with the statistical comparative analysis in the pure and commercial $MgCl_2$-KCl salts, with and without Mg addition, at 850°C for Haynes 230, Haynes NS-163 and Incoloy 800H, respectively.

The corrosion rates with varying Mg concentrations in the salt were plotted against the Mg concentration for each metal, as shown in Figure 37, to understand the trend in the corrosion rate with increasing Mg concentration. All concentrations of Mg tested decreased the corrosion rates for all alloys within the target corrosion rate.

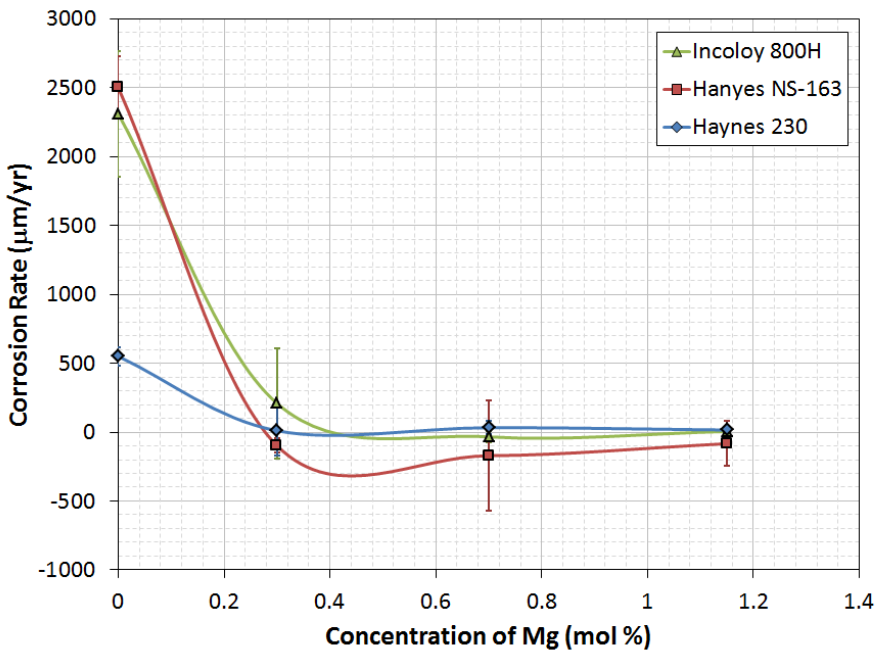

Figure 37. Corrosion rate for alloys with varying Mg concentration at 850°C in commercial $MgCl_2$-KCl.

Task 3.5: Application of Mg Additives to $MgCl_2$ Phase Change Thermal Energy Storage (TES) Systems

Subtask 3.5.2: Evaluation of Corrosion in $MgCl_2$ with Mg during Isothermal and Thermal Cycling

Isothermal and thermal cycling corrosion tests using Incoloy 800-H standard coupons in commercial grade $MgCl_2$, with additions of Mg additive for corrosion control were completed. The corrosion rate results with the statistical comparative analysis are

shown in Table A.10 of Appendix A. A summary of the most relevant results are plotted in Figure 38. Corrosion rates at 850°C in pure and commercial $MgCl_2$-KCl salt are shown for comparison purposes. In general, there are no significant differences in the corrosion rates for Incoloy 800H in the different salts tested. Also, the corrosion rates decrease with decreasing temperature as expected.

The $MgCl_2$ salt melts at 714°C. Consequently, thermal cycling tests were performed by cycling the temperature for 12 hrs at 750°C and 12 hrs at 650°C such that the salt cycles between freezing and melting conditions until 100 hrs have been completed. All the thermal cycling tests with and without the Mg additions showed low corrosion rates. The addition of K-Foam® (Koppers Carbon Foam Grade L1A) increased the corrosion rate of Incoloy 800H and no significant reduction in corrosion was observed when Mg was added to the salt. Since Mg melts at 650°C it may has been possible that the cycling precipitated out the Mg at 650°C, and the Mg could have alloyed with the Ni crucible. However, additional testing is required to understand the results obtained.

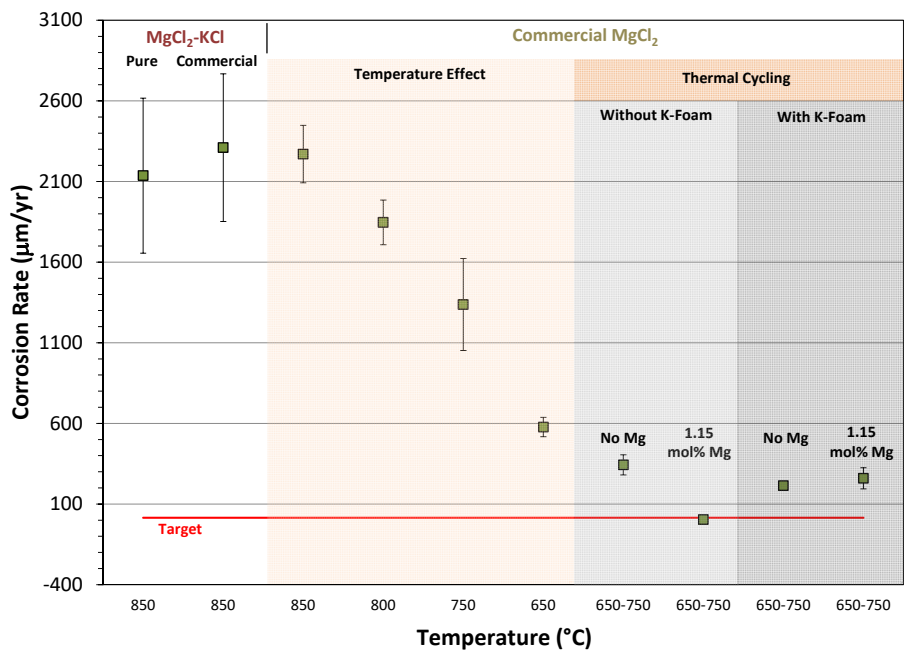

Figure 38. Corrosion rate of Incoloy 800H at different temperatures and under thermal cycling with and without K-Foam in commercial $MgCl_2$.

Subtask 3.5.3-4: Three Dimensional Simulations of Heat, Flow, and Corrosion Inside Thermal Energy Storage System from Argonne National Laboratory

A CFD model was developed for the ANL PCM testing prototype for thermal energy storage (TES) design, The CAD drawing was generated using the PTC Creo parametric 3.0 software. Figure 39 shows the images of the CAD drawings. It is noted that the shape of the thermal energy storage designed in this work is a cylinder. It contains 3 surfaces in contact with molten salt.

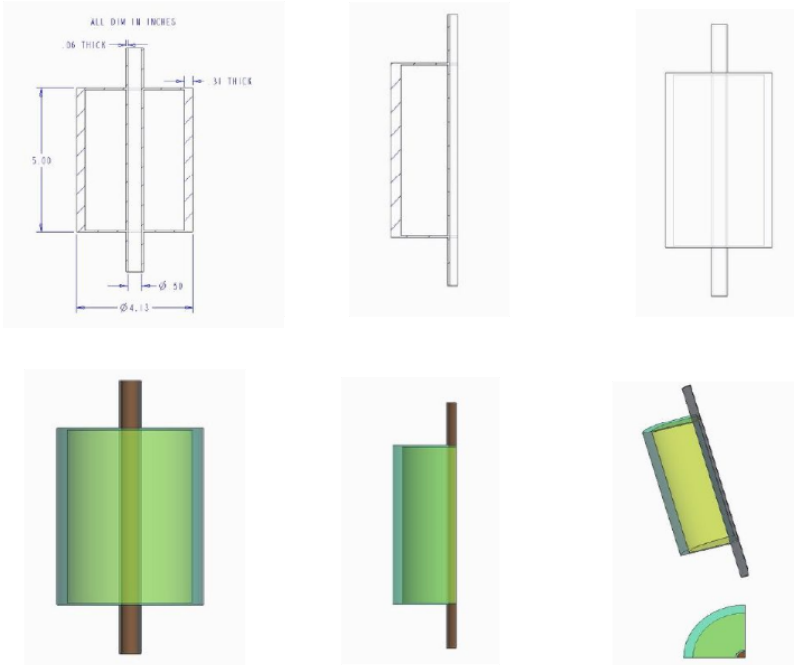

Figure 39. The geometry for thermal energy storage (TES) design from ANL.

From the CAD drawing the computational mesh was exported to the computational fluid dynamics (CFD) package, Star-CD 4.18. The CFD calculations were performed on a quarter section of the geometry since it is axis-symmetric model to increase computational speed. Surfaces 1, 2 and 3 from Figure 40 which show the alloy surfaces in contact with the salt are involved in corrosion reactions. The boundary conditions that were used for preliminary results are shown in Figure 41.The anodic and cathodic reactions are as reactions (21) and (22) and the salt properties, Haynes 230 and Incoloy 800 properties are the same as before [2].

The preliminary results for section plots of temperature gradients, velocity vectors and corrosion rates at the surfaces of alloys (1, 2 and 3 as shown in Figure 40) are shown in Figure 42 and Figure 43, respectively. As the boundary condition for external wall is adiabatic we have almost uniform temperature gradient inside the thermal energy storage. The uniform temperature causes small fluid flow as the density is uniform. SRNL is in communication with ANL to obtain corrosion results when available since ANL's corrosion experiments have been delayed due to a subcontractor move. Comparisons of model predictions with corrosion data from ANL's testing will be made when results are available.

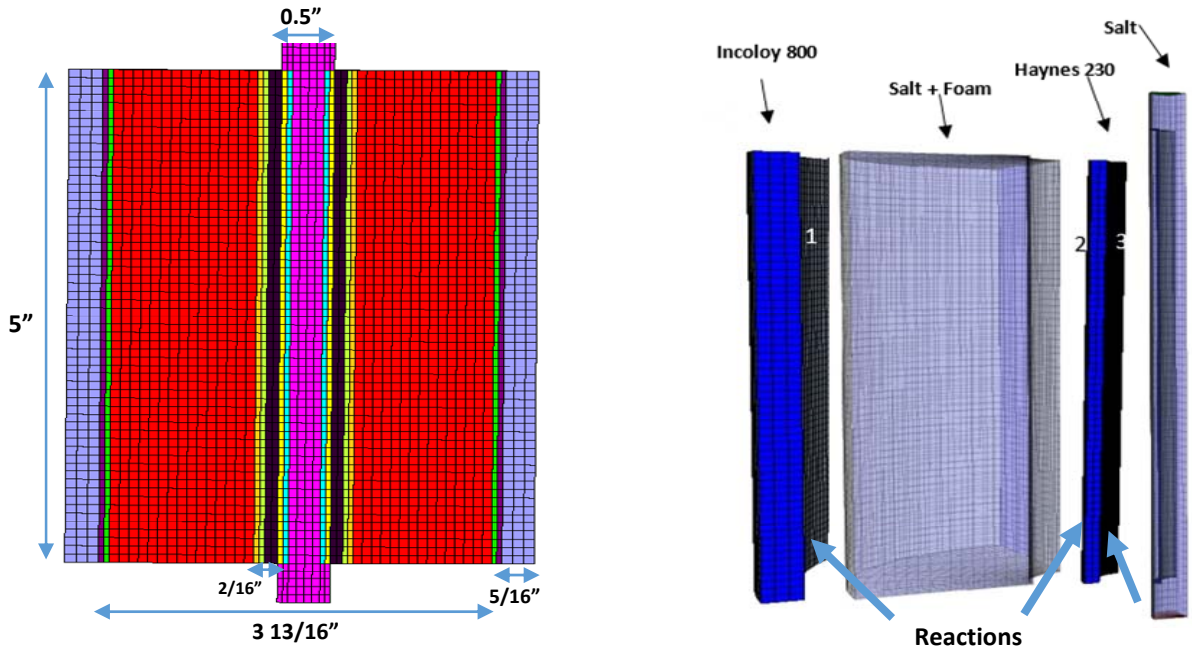

Figure 40. Exported mesh to the computational fluid dynamics (CFD) package, Star-CD 4.18.

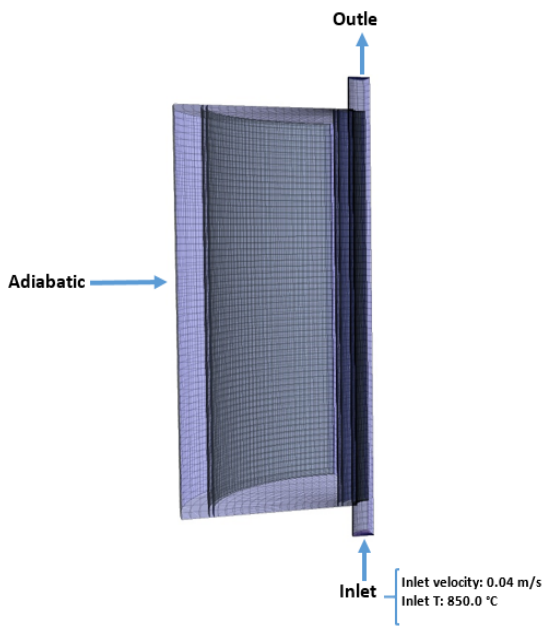

Figure 41. The boundary conditions for thermal energy storage (TES) design from ANL

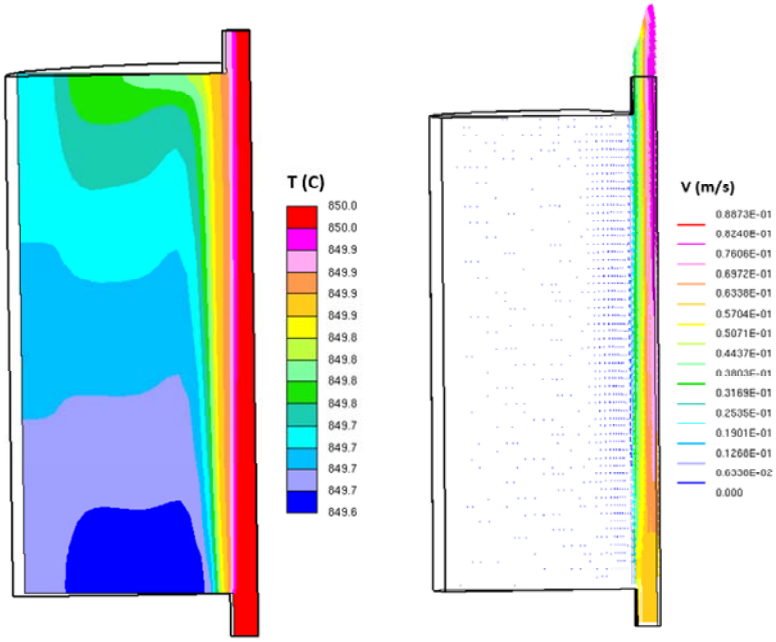

Figure 42. Section plots of the temperature gradients and velocity vectors.

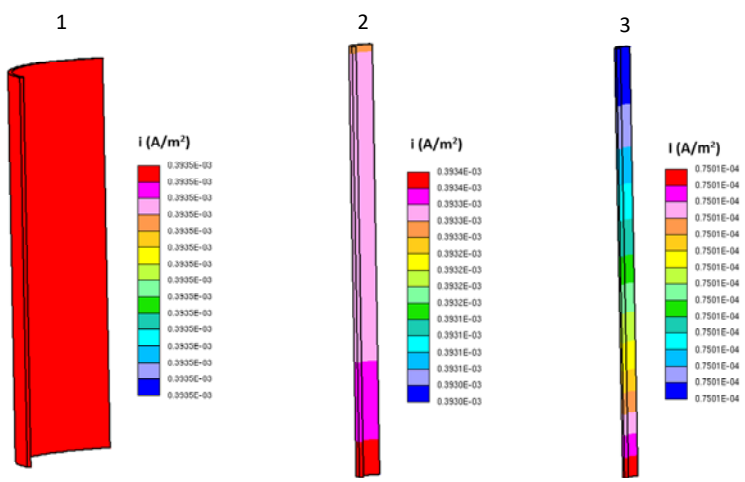

Figure 43. Corrosion rates at the surfaces of alloys (1, 2 and 3 as shown in Figure 40).

Task 3.6: Corrosion Potential Monitoring for Process Control with Mg Corrosion Inhibiting Additive

Corrosion potential monitoring was performed on pure and commercial salt with no added magnesium along with a test where 0.7 mol% of Mg was added to the commercial salt. Figure 44 shows the corrosion potentials relative to the Ag/AgCl reference electrode. The corrosion potentials for the pure and commercial salt with no Mg are both in the range between -0.4 and -0.6 V while the salt containing 0.7 mol% Mg

has a corrosion potential that is much lower at -1.1 V. This potential is below the oxidation potential for Cr and will prevent the Cr from oxidizing.

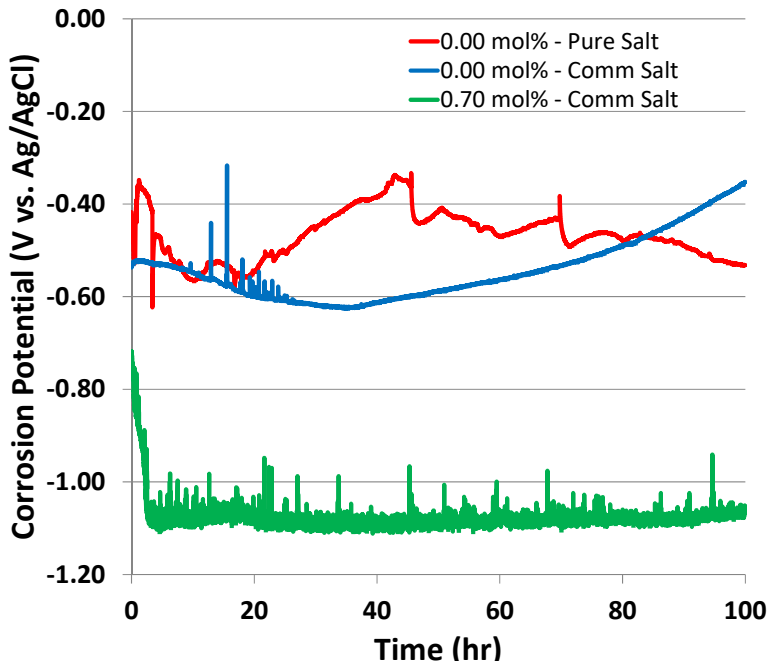

Figure 44. Corrosion potential monitoring for 100 hrs corrosion immersion test of Haynes 230 in commercial and pure KCl-$MgCl_2$ salt with and without Mg at constant temperature

Corrosion potential monitoring for Haynes 230 in commercial $MgCl_2$-KCl salt, with Mg, and under thermal cycling conditions was performed for 100 hrs. Potential and corresponding cycling temperatures are shown in Figure 45. The temperature probe is located in the head space of the reactor which causes the reading to be lower than the actual temperature of the molten salt. Once the salt reached 750°C the electrodes were lowered to monitor the potential during the thermal cycles. In general, the corrosion potentials at 950°C are higher than the potentials at 750°C, but the general trend is that it increases with time until the average potential remains almost constant.

Experiments are being conducted with pure components of the alloys in $MgCl_2$-KCl salt to provide data for corrosion modeling. Figure 46 shows corrosion potential monitoring tests at 850°C for Ni and Cr vs. the Ag/AgCl reference electrode. These measurements show that the potential of the pure Cr metal is around 250 mV lower than the Ni electrode and is more active. This difference in potential provides the driving force for the corrosion reactions in our tests between the Ni Crucible and the Cr rich alloy. The potential difference between the pure Ni and the Cr is similar to the predicted difference in potentials from the thermodynamic modeling. The actual potential differences will be used to provide more realistic values for the electrochemical equilibrium potentials for the alloy components and improve model predictions. The corrosion potential for Cr near -0.48 V is also in the same range as the corrosion potentials for the monitoring

experiments with no Mg in Figure 44. This provides additional indications that Cr is the main oxidation reaction that is occurring on the alloy samples at that potential.

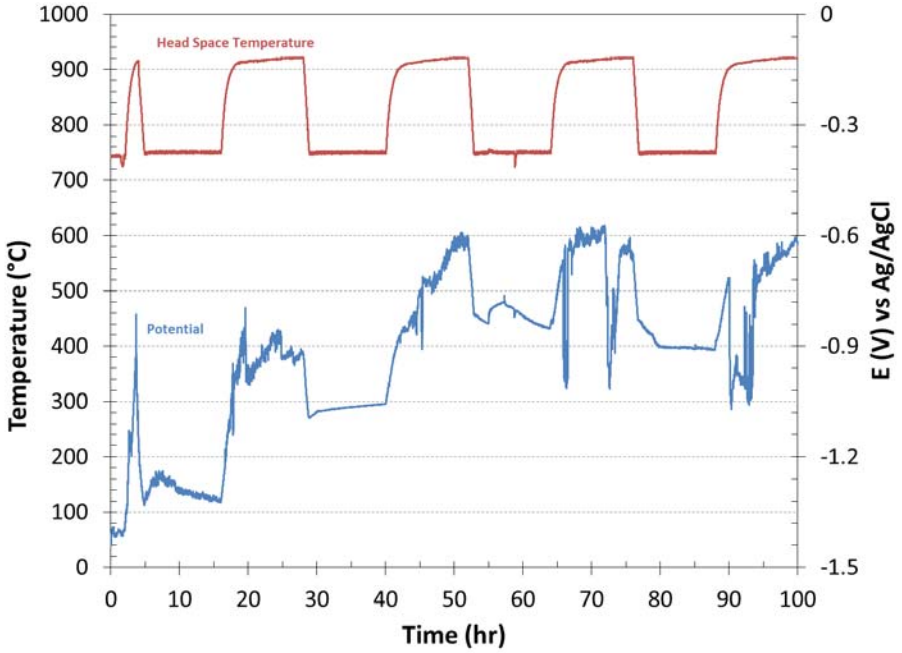

Figure 45. Corrosion potential monitoring for 100 hrs corrosion immersion test of Haynes 230 in commercial $MgCl_2$-KCl salt, with Mg, under thermal cycling conditions.

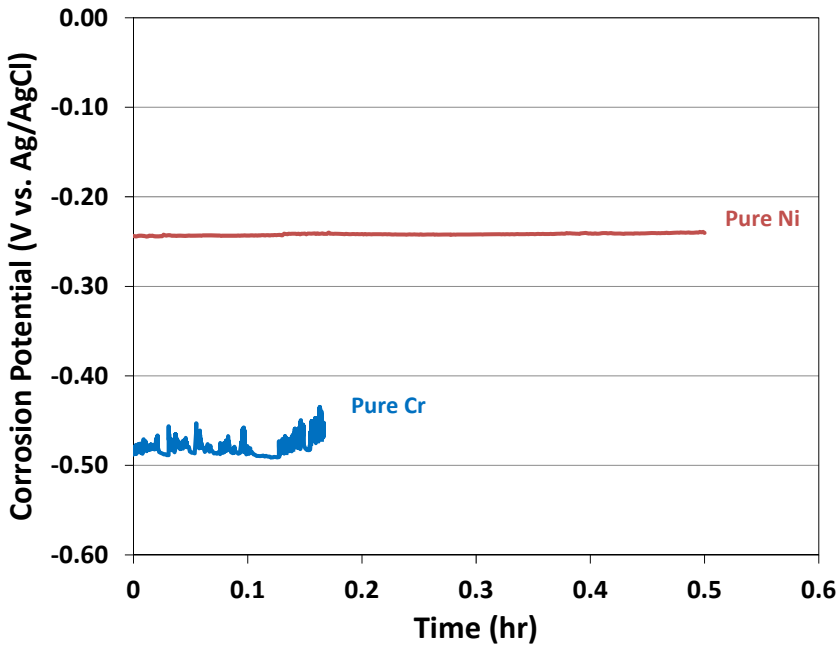

Figure 46. Corrosion potential measurements for Ni and Cr pure metal alloy components in $MgCl_2$-KCl at 850°C.

Conclusions

T-test tables were used for the comparisons of experimental results to determine differences in test results that were statistically significant and these tables are included in the report appendix. Conclusions from the T-test tables were summarized in detail in each section of the report and here is a list of conclusions that apply across the test catagories:

- Differences in corrosion rates in tests with commercial purity salt were not statistically significant from tests with higher purity salt after purification to remove or react moisture impurities was performed.

- In tests with $MgCl_2$-KCl, the addition of Mg decreased the corrosion from cases with no Mg and the corrosion rates were below the DOE SunShot target of 15 μm/yr.

- The corrosion rates for tests with Mg as a corrosion inhibitor in $MgCl_2$-KCl did not have corrosion rates differences that were statistically significant with variation of the Mg content in the salt between 0.3 and 1.15 mol% Mg.

- Tests with welds, U-bends, and welded U-bends showed different corrosion rates and corrosion rates different from the baseline un-welded flat coupon configuration, but the differences in corrosion rates with the addition of Mg were not statistically significant. This indicates that Mg as a corrosion inhibitor will work just as well for these stressed and welded portions of a CSP system.

- The use of Mg as a corrosion inhibitor led to a decrease in the corrosion rate in tests with $MgCl_2$, which indicates this can be an effective method of corrosion inhibition in thermal energy storage systems. The mitigation of corrosion in these thermal energy storage systems using Mg with other components such as carbon foam need to be studied in greater detail to understand how different carbon foam compositions affect the use of Mg as a corrosion inhibitor.

- The mechanical properties Haynes 230 with Mg used for corrosion inhibition remained high after salt exposure. This should be positive for CSP system designers that have identified Haynes 230 as a potential material for high temperature system components due to its mechanical properties.

The following insights are provided to expand on the analysis from the T-test tables with the hope of aiding future use of molten halide salts. Many of the following points are qualitative and based on experimental and theoretical predictions and are predicted to aid in minimizing value lost due to corrosion in a CSP plant. Points may not be applicable in all cases, and some are extrapolations based on the best available knowledge and experience.

- Corrosion will primarily be intergranular for Ni-base, Co-base, and Fe-base alloys, but Fe and Co base alloys will also have more noticeable general surface

attack initially. The primary alloy components that will undergo selective oxidation are Cr and Mn. The species that most readily undergo selective oxidation in molten halides are the ones with the lowest reduction potentials.

- The selective oxidation of Cr from alloys in molten chlorides is mass-transfer limited for alloys with high Cr content (22-27 wt%) and this corrosion rate can be aggravated by increased flow in the system.
- The use of Cr in alloys for the heat transfer system has both positive and negative attributes that have to be considered in designing heat transfer systems that have controlled corrosion
    - Cr is often incorporated at high levels for solid solution strengthening, and airside oxidation resistance in superalloys, but Cr is the principle element attacked in alloys exposed to molten salts with floating redox states, especially when coupled with a high C content in the alloys. Cr is highly reactive in most halide salts and tends to enrich at grain boundaries in the carbide forming temperatures near and above 800 °C, which can lead to devastating grain boundary attack in some alloys without redox controlled salt conditions.
- The presence of gradients in alloy composition and temperature between different parts of the system can aggravate corrosion because of fast reaction kinetics. It has been shown that regions of high nickel content will form NiCr alloy and carbon rich regions can drive formation of chromium carbides.
- The use of industrial grade KCl-$MgCl_2$ salt of similar quality to what can be found in bulk for very low prices could be distinguished from high purity salt after a stepwise heating protocol to react any water absorbed in the salt
- The presence of welds or stresses in the Fe, Ni, or Co based alloys did not cause any additional corrosion mechanisms to occur such as stress corrosion cracking. The following weld types and stress inducing techniques were investigated and did not lead to observable localized corrosion: butt welded flats, U-bends, butt welded U-bends, and fillet welded coupons.
- Corrosion monitoring experiments were consistent in showing that Mg concentrations of 0.3, 0.7, and 1.15 mol% used as a corrosion inhibitor lowers the corrosion potential for alloys to -1.1 V vs. Ag/AgCl at 850°C, which is below the equilibrium potential for Mn and Cr oxidation and therefore should prevent selective oxidation of these alloy components
- Zr can also be used to reduce the corrosion potential in the KCl-$MgCl_2$ system, but some plating of the Zr to form a Ni-Zr alloy was observed and it was unclear if deposition would continue over longer periods of time and restrict flow if used as a corrosion inhibitor. The use of Zr or other metals that can form alloys and create very stable carbides may be a viable way to inhibit corrosion without needing re-addition of a corrosion inhibitor with time, but additional investigation into this would be needed.
- Haynes 230 if used in conjunction with Mg redox control in KCl-$MgCl_2$ is the best choice of current commercially available alloys for most of the high temperature salt facing piping at the highest proposed temperatures of use due to its:
    - thermal fatigue resistance,
    - high creep rupture strength,

  - Ni-base alloying,
  - air side oxidation resistance,
  - high commercial availability in the forms needed for plant fabrication.
- With current generation alloys, any heat transport system that uses chlorides and fluorides will need to have some type of barrier in place to prevent exposure to moisture and oxygen from air.
  - Use of a dried nitrogen or argon cover gas will likely be sufficient to control corrosion due to ingress of atmospheric impurities during routine operation
  - Placement of dried carbon or other sacrificial getters near penetrations of the air boundary may aid in reducing potential corrosion during repairs or other periodic events where the system needs to be opened.
- Most corrosion in chlorides and fluorides is initiated by the presence of impurities such as water, and every effort should be made to reduce these impurities before starting operation of plants.
  - If possible, salts should be purified prior to introducing them to the solar heat transfer system.
  - Moisture and oxygen absorbed from air exposure are the primary contaminants that lead to corrosion. Therefore exposure to water, or oxygen in air should be avoided at all stages, but especially when the salt is in a molten state.
  - Most moisture can be removed by heating the fresh salt components up slowly to drive off physisorbed moisture. Rapid heating of KCl-$MgCl_2(H_2O)$ can lead to boiling of the hexahydrate at ~117 °C.
  - In KCl-$MgCl_2$, or KCl and $MgCl_2$ components, it is ideal to heat to above ~554 °C to drive formation of MgO from hydroxides. Further heating provides a higher thermodynamic driving force for further moisture removal.
  - When heating the salt components to temperature for the first time to dry them, the off-gas may need to be passed through a neutralization filter to capture any evolved HCl. Magnesium hexahydrate may also be evolved and should be expected in the off gas neutralization system.
  - Prior to pumping KCl-$MgCl_2$ into the CSP plant system, the salt should be exposed in its molten state to Mg metal to reduce metal chloride impurities and react remaining HCl.
- Active monitoring of salt redox state is recommended to ensure a corrosion inhibiting state is maintained. An active monitoring system should be possible with cost effective commercially available components.
- Electrochemical testing can provide a rapid and cost effective metric on alloy corrosion susceptibility.

Path Forward

This SunShot project has focused on the use of Mg as a corrosion inhibitor due to its ability to prevent both weight loss and weight gain for alloys in molten chloride systems. It has been shown that as long as the corrosion potential of the alloy remains low that corrosion is inhibited. Therefore, the use of Mg as a corrosion inhibitor necessitates an active corrosion control strategy to ensure that Mg concentration levels are maintained

high enough to inhibit selective oxidation of Cr. The use of Mg was chosen over Zr that forms an alloy with Ni and plates on the alloy surface. SRNL has demonstrated the ability to monitor Mg and implementing a sensor based method to control corrosion should be possible with some additional development for robust sensors. However, industry feedback has favored more passive approaches to corrosion prevention despite the proven ability to meet the DOE corrosion targets using Mg. Additionally, heat transfer system designs that can allow ingress of air or moisture are currently seen very favorably by industry due to familiarity and simplicity for operation.

These industry concerns indicate that the method of corrosion inhibition for the heat transfer systems should be reconsidered. The main concern at the time Mg was chosen as a preferable option to Zr for corrosion inhibition was that Zr may continue plating over time and restrict flow. However, the plating of Zr or another metal that is resistant to oxygen and forms strong carbides could provide a more permanent solution if it is anticipated that the system could be routinely exposed to external impurities. It is also likely that Zr plating will reach an equilibrium thickness and stop plating without obstruction of flow in large diameter tubes.

SRNL has demonstrated the use of in-situ application of coatings based on the rapid electrochemical reactions in molten halide salt systems that have been shown to coat samples over their entire surface even when the coating originates only on one face of a sample. Zr is one example of this, but there are other high temperature materials with high mechanical strength that could be considered and that have been demonstrated by SRNL as part of LDRD projects. Zirconium is known to form very stable passive layers up to 1200°C for nuclear applications and it is likely that by forming alloys with Zr or other materials on the inside of heat transfer systems that their resistance to oxygen or moisture in the molten salt could be increased. The presence of these inhibitors would also form more stable carbides at the grain boundaries of alloys and could help to cut off mass transfer along the grain boundaries that is the fastest degradation pathway. These methods of corrosion inhibition could provide a passive method to prevent corrosion in CSP systems that could be implemented relatively quickly and would be similar in many ways to the Mg corrosion inhibition. Investigation of this method could be done along with exposure testing of the inhibited alloys to salts with air atmospheres or with moist atmospheres. Experimental screening of these coating methods to identify passive corrosion prevention solutions that would be passive and better meet the properties that the CSP industry most wants to see in corrosion inhibition technologies.

References

1. *ASTM G30-97, Standard Practice for Making and Using U-Bend Stress-Corrosion Test Specimens*, 2009.
2. Garcia-Diaz, B.L., *Fundamental Corrosion Studies in High-Temperature Molten Salt Systems for Next Generation Concentrated Solar Power Systems, FY15 Q1, Q2 & Q3 Reports*. 2015,
3. Qiu, J., Y. Zou, G. Yu, H. Liu, Y. Jia, Z. Li, P. Huai, X. Zhou, and H. Xu, *Compatibility of container materials with Cr in molten FLiNaK salt.* Journal of Fluorine Chemistry, 2014. **168**, p. 69-74.

4. Olson, L.C., J.W. Ambrosek, K. Sridharan, M.H. Anderson, and T.R. Allen, *Materials corrosion in molten LiF-NaF-KF salt.* Journal of Fluorine Chemistry, 2009. **130**(1), p. 67-73.
5. Huang, W. and Y.A. Chang, *Thermodynamic properties of the Ni-Al-Cr system.* Intermetallics, 1999. **7**(8), p. 863-874.
6. Chan, K.S., Y.-M. Pan, and Y.-d. Lee, *Development of a First-Principles Computational Methodology for Predicting Long-Term Material Stability and Mechanical Performance, 18-9420*. 2005,
7. Streicher, M.A., *Effect of composition and structure on crevice, intergranular, and stress corrosion of some wrought Ni-Cr-Mo alloys.* Corrosion, 1976. **32**(3), p. 79-93.
8. Popov, B.N., *Corrosion engineering principles and solved problems*. 2015, Elsevier, MA, USA.

Appendix A – T-Test Tables with Individual Conclusions

Introduction

T-test statistical analysis was performed to compare corrosion rate results from different corrosion tests conditions. The conditions that varied during the corrosion tests include salt type, Mg corrosion inhibitor concentration, alloy type, coupon condition, test time, and temperature. Salt tested include pure $MgCl_2$-KCl eutectic mixture, commercial $MgCl_2$-KCl eutectic mixture, and commercial Mg_2Cl. The Mg concentration ranges from 0 to 1.15 mol% in the salt. The tests included three alloys: Haynes 230, Haynes NS-163 and Incoloy 800H. Coupons included flats (standard samples), butt welded flats, U-bends, butt welded U-bends, and fillet welded coupons. These coupons are shown in Figure 16 and Figure 17. The nomenclature used to differentiate the type of coupons is shown in Table 3. Note that each alloy was not tested under all conditions. For example, only Haynes 230 contains corrosion tests with all the stressed coupons types and only Incoloy 800H was tested in the commercial Mg_2Cl.

The following sections in this Appendix organize the T-Test Tables by task. For each task, a table with the T-test analysis is shown for each alloy. Below each table, conclusions regarding the comparison of the corrosion results are listed. In some cases, results are grouped into numbered enclosures that relates to specific conclusions. Unless noted, corrosion rates correspond to 100 hr immersions tests at 850°C.

Each table lists the average corrosion rate along the diagonal (gray cells) with a 95% confidence interval (two times the standard deviations). Corrosion rate comparisons were performed using a significance level of 5% and a two-tailed T-test analysis. The p-values from the T-tests are shown by coloring the cells red for $p < 5\%$ (statistically significant) and green for $p > 5\%$ (not statistically significant), respectively. A dash in a cell indicates that the data for the corresponding test is not available.

Task 3.1: Isothermal Corrosion of Stressed and Welded HTF System Components in Molten Chloride HTFs with and without Mg

Table A.1. Corrosion rates (μm/yr) for Haynes 230 in the pure and commercial $MgCl_2$-KCl salt, with and without Mg addition, at 850°C and comparative statistical analysis.

Haynes 230																						
		Salt	Pure										Commercial									
		mol % Mg	0					1.15					0				1.15					
		Condition	Std	W-Std	U	W-U	Std (TC)	Std	W-Std	U	W-U		Std	W-Std	U	W-U	Std	W-Std	U	W-U	W-U (TC)	W-L
Pure	0	Std	520.3 ± 105.5	0.4%	0.0%	0.0%	2 0.1%	3a 1.6%	0.0%	0.0%	0.0%		1 26.8%	0.0%	0.0%	0.0%	0.0%	0.0%	6 12.3%	0.0%	0.0%	0.0%
		W-Std		429.5 ± 52.5	0.2%	1.4%	0.0%	2.2%	0.1%	0.1%	0.1%		0.8%	0.2%	10.4%	0.5%	0.1%	0.1%	14.7%	0.1%	0.1%	0.2%
		U			205.1 ± 18.7	0.0%	0.0%	9.0%	0.0%	0.0%	0.0%		0.2%	0.1%	0.0%	0.3%	0.0%	0.0%	27.6%	0.0%	0.0%	0.1%
		W-U				313 ± 9.1	0.0%	6.4%	0.0%	0.0%	0.0%		0.5%	0.0%	0.3%	0.0%	0.0%	0.0%	19.9%	0.0%	0.0%	0.0%
		Std (TC)					600.6 ± 63.4	1.7%	0.0%	0.0%	0.0%		9.0%	0.0%	0.0%	0.0%	0.0%	0.0%	10.9%	0.0%	0.0%	0.0%
	1.15	Std						-17.9 ± 96.4	5a 87.8%	42.8%	46.8%		1.0%	25.5%	4.6%	7.7%	4 49.9%	85.7%	86.0%	53.6%	54.3%	24.5%
		W-Std							-11.3 ± 3.8	0.0%	0.1%		0.1%	0.0%	0.0%	0.0%	0.0%	53.1%	82.4%	3.1%	0.4%	0.0%
		U								24.9 ± 5.1	18.8%		0.1%	0.0%	0.0%	0.0%	1.8%	0.0%	65.8%	6.0%	1.0%	0.0%
		W-U									19.6 ± 12		0.1%	0.0%	0.0%	0.0%	37.8%	0.1%	67.9%	14.5%	8.0%	0.0%
Commercial	0	Std											550.2 ± 64.7	0.1%	0.8%	0.3%	3b 0.1%	0.1%	11.5%	0.1%	0.1%	0.1%
		W-Std												62.4 ± 3	0.0%	0.0%	0.0%	0.0%	52.6%	1.6%	0.2%	7.5%
		U													389.8 ± 22.7	0.0%	0.0%	0.0%	16.5%	0.0%	0.0%	0.0%
		W-U														252.5 ± 11.6	0.0%	0.0%	23.6%	0.0%	0.0%	0.0%
	1.15	Std															16.3 ± 5.7	5b 0.1%	69.4%	32.8%	13.4%	0.0%
		W-Std																-10.2 ± 3.3	81.8%	3.3%	0.8%	0.0%
		U																	-44.1 ± 326.8	71.0%	71.3%	51.5%
		W-U																		12.5 ± 6.8	83.0%	0.7%
		W-U (TC)																			11.8 ± 4	0.0%
		W-L																				66.2 ± 4.3

Gray cells in diagonal: average corrosion rate (μm/yr) ± 2σ.
Red cells: p < 5% means that the compared values are statistically significant.
Green cells: p > 5% means that the compared values are not statistically significant.

In general, for 100 hrs tests at 850°C, unless noted as TC (750-950°C),

1. Pure and commercial salts with no Mg in either salt behave differently. However, a notable case is the standard coupon which behaves the same in pure and commercial salt with no Mg in either salt.
2. In the pure salt, corrosion rates under constant temperature and TC conditions are different.
3. Adding Mg to pure and commercial salts change the corrosion rates. The corrosion rates decrease with the addition of Mg.

4. The pure salt with Mg and the commercial salt with Mg behave the same.
5. Coupon conditions change the corrosion rates, except for most of the cases with Mg (5a and 5b).
6. The test for the U-bend coupon in commercial salt with Mg shows no difference with any other test due to its high standard deviation.

Table A.2. Corrosion rates (μm/yr) for Haynes NS-163 in the pure and commercial $MgCl_2$-KCl salts, with and without Mg addition, at 850°C and comparative statistical analysis.

		Salt	Pure			Commercial			
		mol % Mg	0		1.15	0	1.15		
		Condition	Std	Std (TC)	Std	Std	Std	W-U	W-L
Pure	0	Std	2735.9 ± 104.4	0.0%	0.0%	5.1%	0.0%	0.0%	0.0%
Pure	0	Std (TC)		1349.5 ± 522.1	0.0%	0.0%	0.0%	0.0%	0.0%
Pure	1.15	Std			2.1 ± 5.9	0.1%	21.4%	18.6%	60.9%
Commercial	0	Std				2500.2 ± 226.9	0.0%	0.1%	0.0%
Commercial	1.15	Std					-83.1 ± 164.5	19.7%	18.3%
Commercial	1.15	W-U						7.2 ± 4.8	83.5%
Commercial	1.15	W-L							10.4 ± 33.2

Gray cells in diagonal: average corrosion rate (μm/yr) ± 2σ.
Red cells: $p < 5\%$ means that the compared values are statistically significant.
Green cells: $p > 5\%$ means that the compared values are not statistically significant.

In general, for 100 hrs tests at 850°C, unless noted as TC (750-950°C),

1. The standard coupon behaves the same in pure and commercial salt with no Mg in either salt.
2. In the pure salt, corrosion rates under constant temperature and TC conditions are different.
3. Adding Mg to pure and commercial salts change the corrosion rates. The corrosion rates decrease with the addition of Mg.
4. The pure salt with Mg and the commercial salt with Mg behave the same.
5. Coupon conditions change the corrosion rates, except for the cases with Mg.

Table A.3. Corrosion rates (μm/yr) for Incoloy 800H in the pure and commercial $MgCl_2$-KCl salts, with and without Mg addition, at 850°C and comparative statistical analysis.

		Salt	Pure			Commercial					
		mol % Mg	0		1.15	0	1.15				
		Condition	Std	Std (TC)	Std	Std	Std	W-Std	U	W-U	W-L
Pure	0	Std	1991.5 ± 583	15.3%	-----	14.4%	0.0%	0.0%	0.0%	0.0%	0.0%
		Std (TC)		2221.4 ± 61.1	-----	57.4%	0.0%	0.0%	0.0%	0.0%	0.0%
	1.15	Std			-----	-----	-----	-----	-----	-----	-----
Commercial	0	Std				2309.8 ± 458.2	0.3%	0.3%	0.3%	0.3%	0.4%
	1.15	Std					5.2 ± 14	43.3%	1.4%	12.0%	0.0%
		W-Std						1.3 ± 2.6	0.2%	0.0%	0.2%
		U							34.3 ± 3.1	1.8%	0.1%
		W-U								15.7 ± 1.5	0.6%
		W-L									124.6 ± 4.7

Gray cells in diagonal: average corrosion rate (μm/yr) ± 2σ.
Red cells: p < 5% means that the compared values are statistically significant.
Green cells: p > 5% means that the compared values are not statistically significant.

In general, for 100 hrs tests at 850°C, unless noted as TC (750-950°C),

1. The standard coupon behaves the same in pure and commercial salt with no Mg in either salt.
2. In the pure salt, corrosion rates under constant temperature and TC conditions are the same.
3. Adding Mg to commercial salt changes the corrosion rate. The corrosion rate decrease with the addition of Mg. Pure salt with Mg not tested.
4. Coupon conditions change the corrosion rates.

Task 3.2: Measure the Mechanical Properties of Alloys Exposed to $MgCl_2$-KCl and $MgCl_2$-KCl with Mg after Salt Exposure

Table A.4. Corrosion rates (μm/yr) from 100 hr and 500 hr tests for Haynes 230 in the pure and commercial $MgCl_2$-KCl salts, with and without Mg addition, at 850°C and comparative statistical analysis.

		Salt	Pure		Commercial					
		mol % Mg	0	1.15	0			1.15		
		Condition	100 hr	100 hr	100 hr	500 hr	500 hr (TC)	100 hr	500 hr	500 hr (TC)
Pure	0	100 hr	520.3 ± 105.5	1.6%	26.8%	0.1%	0.0%	0.0%	0.0%	0.0%
	1.15	100 hr		-17.9 ± 96.4	1.0%	0.3%	51.5%	49.9%	18.2%	84.7%
Commercial	0	100 hr			550.2 ± 64.7	0.2%	0.1%	0.1%	0.1%	0.0%
		500 hr				799.5 ± 84.3	0.1%	0.1%	0.1%	0.0%
		500 hr (TC)					14.6 ± 0.6	41.3%	0.1%	21.1%
	1.15	100 hr						16.3 ± 5.7	0.0%	19.9%
		500 hr							96.3 ± 10.6	3.1%
		500 hr (TC)								-27 ± 79.2

Gray cells in diagonal: average corrosion rate (μm/yr) ± 2σ.
Red cells: p < 5% means that the compared values are statistically significant.
Green cells: p > 5% means that the compared values are not statistically significant.

In general, for standard coupons on tests at 850°C, unless noted as TC (750-950°C),

1. The standard coupon behaves the same on a 100 hr test in pure and commercial salt with no Mg in either salt.
2. In the commercial salt, corrosion rates under constant temperature from 100 hr and 500 hr tests are different.
3. For the 500 hr tests in commercial salt, corrosion rates under constant temperature and TC conditions are different.
4. Adding Mg to pure and commercial salts change the corrosion rates, except for the 500 hr TC test.
5. For the 100 hr test, the pure salt with Mg and the commercial salt with Mg behave the same.

Table A.5. Corrosion rates (μm/yr) from 100 hr and 500 hr tests for Haynes NS-163 in the pure and commercial $MgCl_2$-KCl salts, with and without Mg addition, at 850°C and comparative statistical analysis.

		Salt	Pure		Commercial			
		mol % Mg	0	1.15	0		1.15	
		Condition	100 hr	100 hr	100 hr	500 hr	100 hr	500 hr
Pure	0	100 hr	2735.9 ± 104.4	0.0%	5.1%	0.0%	0.0%	0.0%
Pure	1.15	100 hr		2.1 ± 5.9	0.1%	0.0%	0.6%	0.8%
Commercial	0	100 hr			2500.2 ± 226.9	0.0%	0.1%	0.1%
Commercial	0	500 hr				591.5 ± 323.5	0.0%	0.0%
Commercial	1.15	100 hr					-35.7 ± 6.2	0.1%
Commercial	1.15	500 hr						23.9 ± 8.7

Gray cells in diagonal: average corrosion rate (μm/yr) ± 2σ.
Red cells: $p < 5\%$ means that the compared values are statistically significant.
Green cells: $p > 5\%$ means that the compared values are not statistically significant.

In general, for standard coupons on tests at 850°C,

1. The standard coupon behaves the same on a 100 hr test in pure and commercial salt with no Mg in either salt.
2. In the commercial salt, corrosion rates under constant temperature from 100 hr and 500 hr tests are different.
3. Adding Mg to pure and commercial salts change the corrosion rates.
4. For the 100 hr test, the pure salt with Mg and the commercial salt with Mg behave differently. However, contrary to other cases this may be due to the weight gain obtained in this test.

Table A.6. Corrosion rates (μm/yr) from 100 hr and 500 hr tests for Incoloy 800H in the pure and commercial $MgCl_2$-KCl salts, with and without Mg addition, at 850°C and comparative statistical analysis.

		Salt	Pure		Commercial			
		mol % Mg	0	1.15	0		1.15	
		Condition	100 hr	100 hr	100 hr	500 hr	100 hr	500 hr
Pure	0	100 hr	1991.5 ± 583	-----	14.4%	38.1%	0.0%	0.0%
Pure	1.15	100 hr		-----	-----	-----	-----	-----
Commercial	0	100 hr			2309.8 ± 458.2	71.5%	0.3%	0.2%
Commercial	0	500 hr				2507.9 ± 1598.8	3.2%	3.2%
Commercial	1.15	100 hr					5.2 ± 13.9	65.5%
Commercial	1.15	500 hr						-10.9 ± 75.4

Gray cells in diagonal: average corrosion rate (μm/yr) ± 2σ.
Red cells: p < 5% means that the compared values are statistically significant.
Green cells: p > 5% means that the compared values are not statistically significant.

In general, for standard coupons on tests at 850°C,

1. The standard coupon behaves the same on a 100 hr test in pure and commercial salt with no Mg in either salt.
2. In the commercial salt, corrosion rates under constant temperature from 100 hr and 500 hr tests are the same.
3. Adding Mg to commercial salt changes the corrosion rates. Pure salt with Mg not tested.

Task 3.4: Isothermal Corrosion in Commercial Purity Molten Chloride HTFs with Mg for Corrosion Control

Table A.7. Corrosion rates (μm/yr) for Haynes 230 in the pure and commercial $MgCl_2$-KCl salts, with different Mg concentrations, at 850°C and comparative statistical analysis.

		Pure		Commercial (Mg in Ni Wire)			
	mol % Mg	0	1.15	0	0.3	0.7	1.15
Pure	0	520.3 ± 105.5	1.6%	26.7%	0.6%	0.0%	0.0%
Pure	1.15		-17.9 ± 96.4	1.0%	67.8%	35.4%	49.9%
Commercial	0			550.2 ± 64.6	0.4%	0.0%	0.1%
Commercial	0.3				10.3 ± 178	71.0%	91.8%
Commercial	0.7					32.7 ± 48.1	35.8%
Commercial	1.15						16.3 ± 5.7

Gray cells in diagonal: average corrosion rate (μm/yr) ± 2σ.
Red cells: p < 5% means that the compared values are statistically significant.
Green cells: p > 5% means that the compared values are not statistically significant.

In general, for the standard coupon on 100 hr tests at 850°C,

1. The pure and commercial salt with no Mg in either salt behaves the same.
2. Adding Mg to pure and commercial salts change the corrosion rates. The corrosion rates decrease with the addition of Mg.
3. The pure salt with Mg and the commercial salt with Mg behave the same.
4. The increase in Mg concentration does not change the corrosion rate. The corrosion rates are not statistically significant.

Table A.8. Corrosion rates (μm/yr) for Haynes NS-163 in the pure and commercial $MgCl_2$-KCl salts, with different Mg concentrations, at 850°C and comparative statistical analysis.

		Pure		Commercial (Mg in Ni Wire)			
	mol % Mg	0	1.15	0	0.3	0.7	1.15
Pure	0	2735.9 ± 104.4	0.0%	5.1%	0.0%	0.1%	0.0%
	1.15		2.1 ± 5.9	0.1%	2.0%	27.4%	21.4%
Commercial	0			2500.2 ± 226.9	0.0%	0.0%	0.0%
	0.3				-98.8 ± 52.3	59.9%	77.9%
	0.7					-170.7 ± 400.6	54.0%
	1.15						-83.1 ± 164.5

Gray cells in diagonal: average corrosion rate (μm/yr) ± 2σ.
Red cells: $p < 5\%$ means that the compared values are statistically significant.
Green cells: $p > 5\%$ means that the compared values are not statistically significant.

In general, for the standard coupon on 100 hr tests at 850°C,

1. The pure and commercial salt with no Mg in either salt behaves the same.
2. Adding Mg to pure and commercial salts change the corrosion rates. The corrosion rates decrease with the addition of Mg.
3. The pure salt with Mg and the commercial salt with Mg behave the same.
4. The increase in Mg concentration does not change the corrosion rate. The corrosion rates are not statistically significant.

Table A.9. Corrosion rates (μm/yr) for Incoloy 800H in the pure and commercial $MgCl_2$-KCl salts, with different Mg concentrations, at 850°C and comparative statistical analysis.

		Pure		Commercial (Mg in Ni Wire)			
	mol % Mg	0	1.15	0	0.3	0.7	1.15
Pure	0	1991.5 ± 583	-----	14.4%	0.0%	0.0%	0.0%
	1.15		-----	-----	-----	-----	-----
Commercial	0			2309.8 ± 458.2	0.0%	0.3%	0.3%
	0.3				208.3 ± 402.2	17.1%	22.2%
	0.7					-33.8 ± 39.6	6.3%
	1.15						5.2 ± 14

Gray cells in diagonal: average corrosion rate (μm/yr) ± 2σ.
Red cells: $p < 5\%$ means that the compared values are statistically significant.
Green cells: $p > 5\%$ means that the compared values are not statistically significant.

In general, for the standard coupon on 100 hr tests at 850°C,

1. The pure and commercial salt with no Mg in either salt behaves the same.
2. Adding Mg to commercial salts changes the corrosion rates. The corrosion rates decrease with the addition of Mg. Pure salt with Mg not tested.
3. The increase in Mg concentration does not change the corrosion rate. The corrosion rates are not statistically significant.

Task 3.5: Application of Mg Additives to $MgCl_2$ Phase Change Thermal Energy Storage (TES) Systems

Table A.10. Corrosion rates (μm/yr) for Incoloy 800H in commercial $MgCl_2$ salt, under thermal cycling and at different temperatures, with different Mg concentrations, and comparative statistical analysis.

			Pure $MgCl_2$-KCl	Commercial $MgCl_2$-KCl	Commercial $MgCl_2$																		
	Temp (°C)		850	850	TC (650-750)	TC (650-750)	TC (650-750)	TC (650-750) - C	TC (650-750) - K	TC (650-750) - K	TC (750-950)	TC (750-950)	TC (750-950)	TC (750-950)	TC (750-950) - C	TC (750-950) - C	850	800	750	750	750	750	650
		mol % Mg	0	0	0	0.3	1.15	0	0	1.15	0	0.3	0.7	1.15	0	1.15	0	0	0	0.3	0.7	1.15	0
Pure	850	0	2136.5 ± 481	1a 41.7%	0.5%	0.4%	0.4%	-----	6a 0.5%	0.5%	0.5%	0.4%	0.4%	0.4%	6b 0.6%	-----	1b 45.3%	16.4%	1.7%	0.4%	0.4%	0.5%	0.7%
Comm	850	0		2309.8 ± 458.2	0.4%	0.3%	0.3%	-----	0.4%	0.4%	0.4%	0.3%	0.3%	0.3%	0.4%	-----	80.5%	6.2%	0.8%	0.3%	0.3%	0.3%	0.5%
Commercial $MgCl_2$	TC (650-750)	0			342.4 ± 62.8	5a 0.2%	0.3%	-----	1.9%	3.3%	0.3%	0.3%	0.3%	0.3%	1.7%	-----	3 1.3%	0.0%	0.0%	0.3%	0.1%	0.5%	0.1%
	TC (650-750)	0.3				18.6 ± 15.6	7.7%	-----	0.0%	0.4%	0.2%	9.0%	25.2%	89.9%	0.1%	-----	1.7%	0.0%	0.0%	36.1%	0.6%	0.4%	0.0%
	TC (650-750)	1.15					3.6 ± 1.7	-----	0.0%	0.5%	0.4%	17.5%	0.0%	0.1%	0.2%	-----	1.8%	0.0%	0.0%	4.3%	3.9%	0.0%	0.1%
	TC (650-750) - C	0						-----	-----	-----	-----	-----	-----	-----	-----	-----	-----	-----	-----	-----	-----	-----	-----
	TC (650-750) - K	0							213.8 ± 5.9	13.8%	8.0%	0.0%	0.0%	0.0%	0.6%	-----	1.9%	0.1%	0.0%	0.0%	0.0%	0.0%	0.2%
	TC (650-750) - K	1.15								258.9 ± 65.3	2.8%	0.5%	0.6%	0.6%	0.2%	-----	1.2%	0.0%	0.0%	0.5%	0.2%	1.1%	0.0%
	TC (750-950)	0									176.5 ± 39.8	5b 0.4%	0.5%	0.5%	} 4a 0.1%	-----	1.6%	0.0%	0.0%	0.4%	0.0%	1.3%	0.0%
	TC (750-950)	0.3										5.2 ± 4.8	0.1%	0.0%	0.2%	-----	1.8%	0.0%	0.0%	5.0%	3.4%	0.0%	0.1%
	TC (750-950)	0.7											11.5 ± 3.9	0.1%	0.2%	-----	1.8%	0.0%	0.0%	52.8%	2.4%	0.0%	0.1%
	TC (750-950)	1.15												19.3 ± 3.2	0.2%	-----	1.8%	0.0%	0.0%	9.5%	1.6%	0.0%	0.1%
	TC (750-950) - C	0													443.6 ± 63.4	-----	1.3%	0.0%	0.0%	0.2%	0.1%	0.2%	0.6%
	TC (750-950) - C	1.15														-----	-----	-----	-----	-----	-----	-----	-----
	850	0															2270 ± 178.2	3.7%	0.2%	1.8%	1.6%	1.8%	2b 1.5%
	800	0																1846.3 ± 137.9	0.0%	0.0%	0.0%	0.1%	0.0%
	750	0															2a		1337.5 ± 285	5c 0.0%	0.0%	0.0%	} 4b 0.0%
	750	0.3																		13.2 ± 7.7	1.5%	0.0%	0.1%
	750	0.7																			-26.9 ± 21.8	0.3%	0.0%
	750	1.15																				78.5 ± 2.9	0.1%
	650	0																					576.7 ± 60.2

Gray cells in diagonal: average corrosion rate (μm/yr) ± 2σ.
Red cells: $p < 5\%$ means that the compared values are statistically significant.
Green cells: $p > 5\%$ means that the compared values are not statistically significant.

Notes:
C = Duocel® Reticulated Vitreous Carbon (RVC) Foam with100 PPI and a porosity of 91%.. Non-graphite.
K = K-Foam® (Koppers Carbon Foam Grade L1A) with a porosity of 78%. Graphite.

In general, for the standard coupons on 100 hr tests,

1. All three salts tested (pure and commercial salts) with no Mg in either salt behaves the same.

In general, for the standard coupon on 100 hr tests in the commercial $MgCl_2$ salt,

2. The increase in temperature increases the corrosion rates, except for the TC tests.
3. Corrosion rates under constant temperature and TC conditions behave differently.
4. Adding Mg to the salt changes the corrosion rates, except for the TC test (650-750°C) with K-Foam. The corrosion rates decrease with the addition of Mg. TC (750-950°C) with C-Foam (RVC) and Mg not tested.
5. The increase in Mg concentration changes the corrosion rate.
6. The addition of carbon foam (RVC or K-Foam) changes the corrosion rate.